TTMP
ISSN:3041-8984

Transactions in Theoretical and Mathematical Physics

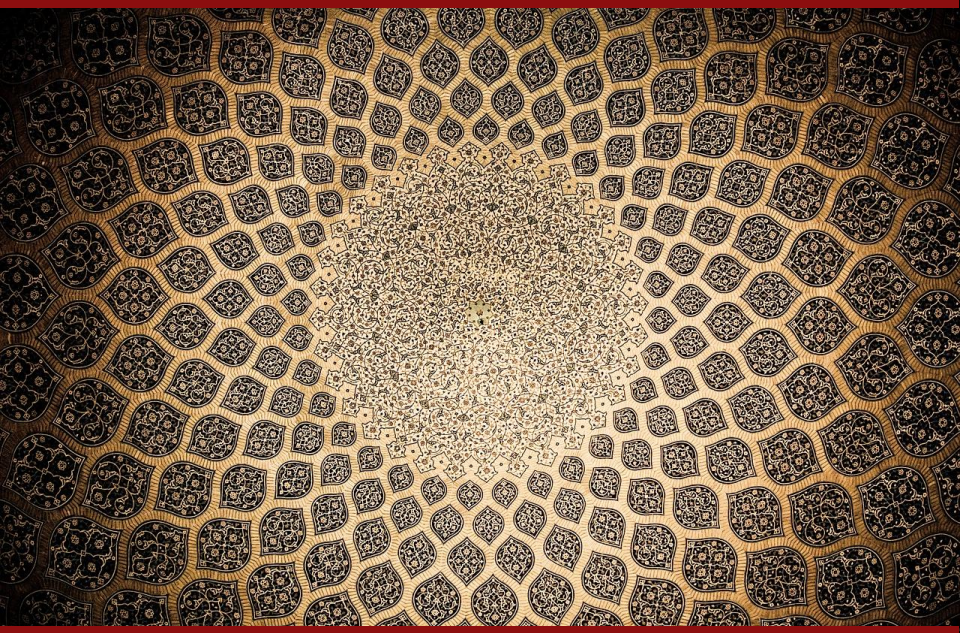

Volume 3 (2) 2026
Available Online at: https://ttmp.qut.ac.ir

Transactions in Theoretical and Mathematical Physics

Publisher: Qom University of Technology

ISSN: 3041-8984

Volume**:** 3, Issue 2, 2026

Available online: https://ttmp.qut.ac.ir

Table of Contents

TTMP vol 3 (2), 2026
doi: 10.30511/TTMP.2026.2087762.1074

Transactions in Theoretical and Mathematical Physics

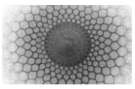

Hybrid FEM-RBFNN: A Fusion of Finite Element Method and Radial Basis Function Neural Networks for Solving PDEs

R.O. Ojo[1a], A.F. Adebisi[1], T.O. Ganiyu[1], M.O. Ogunniran[1], M. Bayram[3], K.O. Kareem[2]

[1] Department of Mathematical Sciences, Osun State University, Osogbo, Nigeria
[2]Department of Mathematical Sciences, Federal College of Education, Iwo, Nigeria
[3]Faculty of Engineering, Biruni University, Turkey

Received: 29 March 2026 / Accepted: 03 April 2026/ Published: 04 May 2026

Abstract The Finite Element Method (FEM) serves as a standard numerical technique for Partial Differential Equation (PDE) solutions because it maintains stability combined with theoretical proof. The method experiences significant performance issues when dealing with high-dimensional spaces that require fine mesh resolutions. The research introduces a hybrid FEM-RBFNN framework that serves as a fast surrogate model for studying nonlinear wave motion. The hybrid method uses Radial Basis Function Neural Network (RBFNN) training on low-cost, coarse-grid FEM data to produce accurate results without requiring full-mesh refinement. The nonlinear Schrödinger Equation (NLSE) analysis shows that FEM-RBFNN successfully tracks the movement of complex solitons while mitigating numerical issues arising from coarse mesh grids. The results demonstrate that the system achieves a 60× speedup over detailed ground-truth simulations, reducing processing time from 4.60s to 0.08s. The surrogate maintains an L_2 error of 0.014, matching the performance of the coarse source while using training data to address high-frequency dispersive tails. The research develops an efficient PDE solver that supports real-time simulations and extensive parameter exploration through its robust, differentiable features.

Keywords: Finite Element, Nonlinear Schrödinger Equation, Radial Basis Function, Neural Networks.

1 Introduction

Fundamental in nature, partial differential equations help simulate complex phenomena across several scientific and technological domains. Computational meshes are fundamental to the accuracy and stability of traditional numerical methods such as the Finite Element Method (FEM), Finite Difference Method (FDM), and Finite Volume Method (FVM). These techniques nevertheless struggle with dynamic boundaries and complex geometries, where mesh generation becomes computationally costly. Eliminating meshing limitations enables mesh-free methods, especially neural network-based systems such as Physics-Informed Neural Networks (PINNs) and Radial Basis Function Neural Networks, to serve as a potential substitute [1]. Although neural networks are perfect universal approximators, their convergence guarantees and numerical stability remain the subject of ongoing study. Numerical methods for PDEs have been enhanced by recent developments, including the rational multi-derivative integrator by [2]. This work presents a hybrid FEM-RBFNN framework integrating the stability of FEM with the adaptability of RBFNNs to improve solution accuracy and computational efficiency. Particularly in cases with noisy or inadequate data, the suggested method is meant to manage both stationary and time-dependent PDEs.

FEM's efficiency in solving PDEs does not eliminate problems, including high computational cost, numerical instability, and the need to handle irregular domains. Although RBFNNs have shown promise in enhancing numerical methods through improved function approximation and generalisation [3], their integration with FEM remains a challenging area of ongoing research. This work aims to provide a hybrid FEM-RBFNN framework to address computational inefficiencies, improve mesh discretisation, and enhance numerical stability while preserving high solution accuracy. The results will help to advance hybrid numerical approaches for the solution of challenging PDEs in several fields [4, 5].

The research develops a hybrid numerical framework combining FEM and RBFNNs that improves the accuracy, efficiency, and flexibility of PDE simulations. The framework provides an efficient computational method that adapts to solve difficult PDE problems through a combination of

[a]ojoridwan001@gmail.com

numerical methods and machine learning techniques. The combination of FEM with Radial Basis Function Neural Networks is necessary because FEM struggles with specific problems involving noisy data, complex geometries and domains, and the need for local adaptivity and improved solution smoothness. The integration allows generalisation because PDE problems are partially defined by boundary data deficiencies and undisclosed coefficient information. The hybrid technique aims to enhance FEM performance in challenging problem situations while preserving its existing functionality.

This study presents a hybrid FEM-RBFNN framework that improves numerical resolution of PDEs by combining FEM and RBFNN techniques. RBFNNs enhance numerical accuracy through their ability to diminish numerical errors, which leads to better FEM solutions for PDEs. The hybrid model achieves greater computational efficiency through shorter solution times, enabling its use in extensive simulations. This method successfully solves nonlinear PDEs, complex geometric structures, and difficult boundary conditions in complex domains, which pose challenges for traditional FEM methods [6]. RBFNNs enhance FEM approximation accuracy through their capacity to model geometric variations while maintaining the fundamental properties of FEM [7]. The method improves observational data integration by applying it to real-world situations that include sparse or noisy data, thereby supporting the solution of inverse problems [4, 5].

PDEs admit both analytical and numerical solution methods. The mathematical techniques of integral transformations and separation of variables enable analytical methods to deliver exact solutions for simple PDEs and geometric problems, but their application is limited to these basic situations. In complex situations, numerical techniques that approximate PDE solutions using computer methods are therefore more sensible. By discretising the problem domain and approximating derivatives using difference equations [8], the finite difference method is used. Stability restrictions cause FDM to struggle with complex domains and high-dimensional problems, even though it is theoretically simple and computationally economical for simple geometries [7]. With piecewise polynomials, the FEM approximates solutions and is therefore appropriate for irregular geometries and complex boundary conditions [6]. Its localised basis functions produce sparse system matrices that improve computational efficiency; however, mesh generation can be computationally costly. Because it guarantees local conservation of mass, energy, and momentum, the finite-volume method is frequently employed for PDEs originating from conservation laws. In computational fluid dynamics, FVM is extensively used; precise flux computations in irregular geometries can be difficult. With excellent accuracy, spectral methods approximate solutions using orthogonal basis functions, such as Chebyshev polynomials or Fourier series [9]. But the Gibbs phenomenon causes them problems with discontinuities and irregular domains. Computational accuracy and efficiency are highly influenced by the choice of basis functions and the mesh resolution.

2 Finite Element Method

Especially in complex domains, FEM is a commonly used numerical method for solving PDEs. Using localised basis functions [10] defined in small subregions known as finite elements, it approximates solutions. The approach transforms PDEs into a variational form, thereby generating algebraic equations that can be solved using matrix techniques. FEM's advantage lies in its ability to produce sparse system matrices, thereby improving computational efficiency. Adaptive mesh refinement, which enables higher resolution in important areas such as steep gradients or singularities, is a vital component of FEM [11]. However, mesh generation, especially in three dimensions, remains computationally intensive [6]. FEM has significant applications across many fields. Stress analysis and vibration simulations find application in structural engineering. FEM models the Navier-Stokes equations for both aerodynamic and biological uses in fluid dynamics. Heat transfer is achieved through two methods: thermal conduction and radiation simulation. The finite element method FEM is used in geophysics to model seismic wave propagation and groundwater movement, while it serves as a tool for solving Maxwell's equations in antenna and waveguide designs. The field of biomedical engineering uses FEM to create biomechanical models which examine stress distribution in both bones and prosthetic devices. The technology is used in acoustics for its ability to control noise and study sound wave motion. The finite element method FEM remains an effective tool for solving partial differential equations PDEs because it provides precise solutions through its performance in various scientific and engineering fields, despite facing challenges from high computation requirements and intricate mesh structures.

2.1 Artificial Neural Networks

Artificial neural networks (ANNs) serve as universal approximators, unlike traditional linear techniques. The system uses biological neural networks as its basis to build interconnected layers of neurons that identify data patterns and relationships for classification, regression, and function approximation tasks. Neural networks utilise connections with assigned weights to process information. The neuron receives multiple inputs and performs a weighted sum before applying a non-linear activation function to produce an

output, which is then forwarded to other neurons. The mechanism enables ANNs to learn complex relationships which include non-linear patterns [12]. The training process uses weight adjustments via optimisation algorithms, such as gradient descent, to reduce prediction errors. The structure of ANNs consists of an input layer and multiple hidden layers that lead to an output layer. Data in hidden layers extract their most abstract features, which then lead to predictions. The selection of activation functions, along with architectural design and training approaches, determines how well the system performs. The three major activation functions used in neural networks include sigmoid, hyperbolic tangent, and Rectified Linear Unit (ReLU). Each neural network type serves a specific data processing purpose. Convolutional Neural Networks (CNNs) prove most effective at processing images, while Recurrent Neural Networks (RNNs) function best with sequential data [13]. Physics-Informed Neural Networks use physical laws as training elements, while Radial Basis Function Neural Networks utilise radial basis functions to achieve precise function approximation results. The basic form of artificial neural networks, the Feedforward Neural Network (FFNN), transmits data in a single direction [14]. The Universal Approximation Theorem shows that any continuous function can be approximated by a fully connected FFNN when the network reaches enough depth or width [12]. PINNs use physical constraints integrated into their loss functions to solve partial differential equations while reducing their reliance on labelled data. RBFNNs achieve excellent accuracy in function approximation and interpolation because their radial basis functions reach fast convergence times with smooth function approximations [15]. The dissertation evaluates RBFNNs for their efficient operation, with strong approximation performance as its primary focus. The chosen architectures will meet the required approximation accuracy standards demanded by the studied tasks.

Figure (1) illustrates the conceptual analogy between a biological neuron and an artificial neuron, which serves as the foundational building block of artificial neural networks. In the biological setting, a neuron uses structures known as dendrites to receive signals from neighbouring neurons. After processing these signals in the cell body, the neuron produces an electrical impulse that travels down the axon and connects with other neurons through synapses when the total input exceeds a predetermined threshold. The left side shows how an artificial neuron replicates this process through mathematical representation. It receives multiple numerical inputs, each multiplied by an associated weight. The combination of weighted inputs with the bias term creates a value that the activation function uses to determine the neuron's output. This output can then serve as input to other neurons in the network.

The resemblance between biological and artificial neurons highlights the inspiration drawn from neuroscience in the design of neural networks. Artificial neurons create predictive patterns through training by modifying weights and biases, enabling the system to perform predictive and classification tasks and to recognise complex relationships in data, just as the human brain develops knowledge through life experiences.

2.2 Radial Basis Function Neural Networks (RBFNNs) – Fundamentals and Applications

Radial Basis Function Neural Networks are a class of artificial neural networks widely used in regression, classification, function approximation, and time-series forecasting. Designed in the late 1980s, RBFNNs are prized for their simple architecture, fast learning, and ability to represent complex, nonlinear interactions. Three layers comprise them: an input layer, a hidden layer with radial basis activation functions (often Gaussian), and a linear output layer. The hidden layer computes distances between inputs and neuron centroids by underlying localised activation and effective function approximation. Three fundamental parameters (centres, spreads, and output weights) are optimised during RBFNN training. While spreads are often calculated using heuristics such as the mean distance to the nearest neighbour, centres are usually found using clustering techniques such as K-means or random sampling. Commonly used for output weights, the least squares estimate streamlines training. RBFNNs have a main benefit of fast training because they do not require deep backpropagation. Rather, they employ a two-phase approach: first computing output weights [15], then deciding centres and spreads. This structure lowers computational cost and allows fast convergence. In function approximation, interpolation, and pattern recognition, RBFNNs shine. They are used in time-series forecasting for energy modelling, weather prediction, and financial markets, as well as in classification tasks such as image recognition, medical diagnosis, and biometric identification. They are also rather important. Adaptive control systems, system identification, and signal processing also make use of RBFNNs. Especially in solving partial differential equations, RBFNNs have shown potential as substitutes for conventional numerical techniques such as the FEM and the Finite Difference Method. The smooth interpolation method, together with its capacity to handle complex geometric shapes through direct modelling without using mesh systems, makes this technique highly useful for structural analysis, fluid dynamics and heat transfer applications. The method faces three main problems: sensitivity to parameter selection, potential overfitting, and increased computational demands associated with high-dimensional data. The research examines the integration of RBFNNs with FEMs

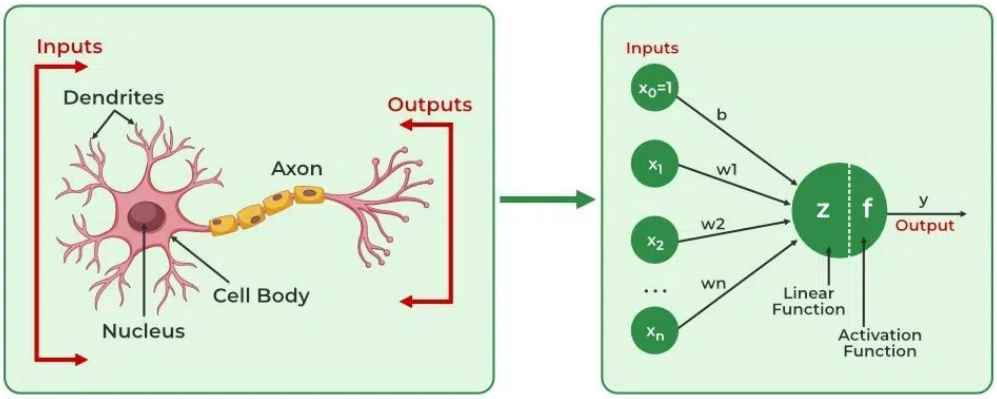

Fig. 1 Illustration and Comparison of a Biological Neuron and an Artificial Neuron

to improve the numerical stability and computational performance of PDE solution methods.

2.3 Hybrid and Machine Learning-Based Methods

The evolution of computational science has created hybrid methods which combine neural network technology with established numerical techniques to solve PDEs. The research work of [16, 17] employed neural networks as priors within a finite element framework to achieve stability improvements by reducing the need for explicit regularisation. The research of [18] provided a foundation for further research, enabling scientists to solve inverse problems with enhanced accuracy, though the process required increased computational power.

The research of [2] presented a rational multi-derivative integrator which solves singular and advection equations by using adaptive residual subsampling to manage computational needs. The research work of [19] developed a hybrid block method that solves singular initial value problems using Poisson, collocation, and interpolation power series techniques to improve numerical stability.

The research work of [20] developed a hybrid framework that integrated neural networks with block integrators to enhance solutions to boundary value problems, achieving better performance and greater accuracy. The research demonstrates how hybrid methods can combine traditional numerical solvers with machine learning techniques to create powerful solutions for PDE problems.

2.4 Comparative Analysis of Existing Methods

The Finite Difference Method, Finite Element Method, and Finite Volume Method, which are traditional numerical methods for solving partial differential equations, face challenges when applied to advanced problems involving complex geometries and multidimensional spaces, and they require expensive computational resources. RBFNNs and PINNs, among other neural network-based methods, offer better function approximation. However, RBFNNs are sensitive to hyperparameters, and PINNs demand large computational resources. The goal of hybrid methods is to combine the advantages of numerical and neural network techniques. Although they may cause more computing overhead, methods including FEM-NN hybrids and neural network-enhanced integrators have shown higher accuracy and adaptability. The growing number of studies on hybrid approaches highlights their ability to create more accurate and effective PDE-solving systems.

3 Mathematical Formulation and Problem Definition

3.1 Finite Element Method

3.1.1 Weak Formulation of the Governing Equation

The finite element method is based on deriving the weak form of a governing partial differential equation. Consider a general second-order PDE given by

$$-\nabla \cdot (a(x)\nabla u(x)) = f(x), \quad x \in \Omega, \tag{1}$$

subject to the boundary conditions:

$$u(x) = g(x), \qquad x \in \partial\Omega_D, \tag{2}$$

$$a(x)\frac{\partial u}{\partial n} = h(x), \qquad x \in \partial\Omega_N. \tag{3}$$

Table 1 Comparison of Existing Methods for Solving PDEs

Method	Strengths	Limitations	Applications
Finite Difference	Simple, efficient for regular grids	Struggles with complex geometries, stability issues	Heat transfer, wave equations
Finite Element	Handles complex geometries, high accuracy	Computationally intensive, complex meshing	Structural analysis, fluid dynamics
Finite Volume	Conservation laws, flexible meshing	Lower-order accuracy, complex flux approximations	Fluid dynamics, heat transfer
RBFNN	Smooth interpolation, good for non-linear relationships	Sensitive to hyperparameters, scalability issues	Function approximation, spatial interpolation
PINNs	Physics-based learning, solves inverse problems	High training cost, convergence challenges	Scientific computing, data-scarce environments
Hybrid Methods	Combines strengths of traditional and neural approaches	Increased complexity, potential stability issues	Inverse problems, real-time simulations

The weak formulation is obtained by multiplying the equation by a test function $v(x)$ and integrating over the domain, we obtain:

$$\int_{\Omega} v(x)\left(-\nabla\cdot(a(x)\nabla u(x))\right)dx = \int_{\Omega} v(x)f(x)\,dx. \tag{4}$$

Using integration by parts and applying boundary conditions, we derive the weak form:

$$\int_{\Omega} a(x)\nabla v(x)\cdot\nabla u(x)\,dx - \int_{\partial\Omega_N} v(x)h(x)\,d\Gamma = \int_{\Omega} v(x)f(x)\,dx. \tag{5}$$

3.2 FEM Discretisation Strategy

The domain Ω is discretised into finite elements, and the unknown function $u(x)$ is approximated as:

$$u(x) \approx \sum_{i=1}^{n} u_i\phi_i(x), \tag{6}$$

where: u_i represents the unknown nodal values, and $\phi_i(x)$ are the shape functions.

Substituting this into the weak form leads to the system of equations:

$$\mathbf{Ku} = \mathbf{f}, \tag{7}$$

where:

$$\mathbf{K}_{ij} = \int_{\Omega} a(x)\nabla\phi_i(x)\cdot\nabla\phi_j(x)\,dx, \tag{8}$$

$$\mathbf{f}_i = \int_{\Omega} \phi_i(x)f(x)\,dx + \int_{\partial\Omega_N} \phi_i(x)h(x)\,d\Gamma. \tag{9}$$

3.2.1 Solution of PDE from FEM

Solving the system $\mathbf{Ku} = \mathbf{f}$ yields the nodal values:

$$\mathbf{u} = [u_1, u_2, \ldots, u_n]. \tag{10}$$

where $\mathbf{K}$ is the stiffness matrix, $\mathbf{u}$ is the vector of unknown nodal values, and $\mathbf{f}$ represents external forces or source terms.

These nodal solutions ($\mathbf{u}$) serve as training data for the Radial Basis Function Neural Network.

3.3 Justification for Hybridising FEM and RBFNN

FEM depends on mesh quality and has a high computational cost, whereas RBFNNs are mesh-free with better generalisation. Hybridising FEM with RBFNN allows leveraging FEM's numerical rigour while enhancing flexibility and efficiency through RBFNNs.

3.4 Conceptual Framework of the Hybrid Model

To raise the accuracy and efficiency of partial differential equation solving, the hybrid model combines Radial Basis Function Neural Networks with the Finite Element Method. By means of nodal value solving, FEM discretises the problem domain and generates an initial approximation. FEM solutions, however, might be sensitive to mesh quality and require fine discretisation to achieve high accuracy, thereby increasing computational cost. The RBFNN system functions as a post-processing tool which enhances the results of the FEM analysis. The neural network learns from FEM nodal solutions using spatial coordinates, producing outputs that match FEM results. RBFNN achieves better solution

accuracy through its interpolation and generalisation abilities, which do not require additional mesh development. The numerical framework of FEM benefits from this method's structured organisation, while RBFNN serves as a tool that reduces errors and produces smoother results. The hybrid model enables efficient computation while maintaining accuracy by solving complex geometric problems that require more FEM refinements to achieve the same level of precision.

3.5 Integration of FEM and RBFNN

3.5.1 Training the RBFNN

The data for training the RBFNN is extracted from the FEM results:

- Input (X): Nodal coordinates, material properties, and boundary conditions.
- Output (Y): FEM-computed unknowns (e.g., displacements, stresses, or temperatures).

The training dataset is structured as:

$$\{(X_i, Y_i)\}, \quad i = 1, 2, \ldots, n, \tag{11}$$

where:

$$X_i = [x_{i1}, x_{i2}, \ldots, x_{im}], \tag{12}$$

$$Y_i = [u_{i1}, u_{i2}, \ldots, u_{ip}] \tag{13}$$

3.6 Radial Basis Function Neural Network (RBFNN) Enhancement

To refine the FEM solution, RBFNN is employed as a post-processing tool. Given a set of nodal coordinates $X = \{x_1, x_2, \ldots, x_n\}$ and their corresponding FEM-computed values $Y = \{u_1, u_2, \ldots, u_n\}$, RBFNN approximates the solution as:

$$\tilde{u}(x) = \sum_{i=1}^{n} w_i \phi(\|x - c_i\|), \tag{14}$$

where $\phi(r)$ is a radial basis function and $r = \|x - c_i\|$ is the Euclidean distance

3.6.1 Radial Basis Function

The choice of radial basis function affects the accuracy of the approximation. Commonly used functions include:

$$\phi(r) = \exp\left(-\frac{r^2}{2\sigma^2}\right), \qquad \text{Gaussian,} \tag{15}$$

$$\phi(r) = \sqrt{r^2 + \sigma^2}, \qquad \text{Multiquadric,} \tag{16}$$

$$\phi(r) = \frac{1}{\sqrt{r^2 + \sigma^2}}, \qquad \text{Inverse Multiquadric.} \tag{17}$$

where σ is the spread parameter.

3.6.2 Computation of Weights

The weights w_i are determined by solving the linear system:

$$\Phi W = Y, \tag{18}$$

where Φ is the interpolation matrix with entries:

$$\Phi_{ij} = \phi(\|c_i - c_j\|), \tag{19}$$

and $W = [w_1, w_2, \ldots, w_n]^T$, $Y = [u_1, u_2, \ldots, u_n]^T$.

3.6.3 RBFNN Output

The output of the RBFNN is given by:

$$\hat{Y} = \sum_{i=1}^{m} w_i \phi(\|X - c_i\|) + b, \tag{20}$$

where w_i represents the weight of the i-th RBF, c_i is the centre of the i-th RBF, b is the bias term, m is the number of RBF centres.

3.6.4 Optimisation of RBFNN Parameters

To achieve optimal performance, parameters w_i, c_i, and σ are optimized by minimizing the error function:

$$\text{Error} = \frac{1}{2} \sum_{i=1}^{n} \|Y_i - \hat{Y}_i\|^2. \tag{21}$$

Using techniques such as gradient descent or least squares fitting, the weights and spread parameters are updated iteratively to minimise the error.

3.6.5 Prediction Using RBFNN

For new input data X_{new}, the trained RBFNN predicts the unknowns as:

$$Y_{\text{new}} = \sum_{i=1}^{m} w_i \phi(\|X_{\text{new}} - c_i\|) + b. \tag{22}$$

3.7 Purpose and Role of the RBFNN in the Hybrid FEM–RBFNN Framework

The Finite Element Method is a powerful numerical tool for solving partial differential equations by discretising the problem domain $\Omega \subset \mathbb{R}^n$ into smaller elements. However, the accuracy of FEM strongly depends on mesh resolution, and refining the mesh significantly increases computational cost. To overcome this limitation, we propose coupling FEM with a Radial Basis Function Neural Network, forming a hybrid framework that leverages the physical rigour of FEM and the approximation power of neural networks. The RBFNN acts as an adaptive post–processor to the coarse–mesh FEM solution. Rather than attempting to reproduce the coarse–mesh results, the network learns a continuous functional mapping from the spatial coordinates to the PDE solution and produces a smoother, mesh–independent approximation that can generalise to arbitrary points in Ω. Let $u(x)$ denote the exact solution of a PDE in Ω, and let $u_h(x)$ represent the FEM approximation on a coarse mesh $\mathscr{T}_h$. The hybrid strategy aims to construct a continuous surrogate $\hat{u}(x)$ satisfying

$$\hat{u}(x) \approx u(x), \quad \forall x \in \Omega,$$

The RBFNN model requires training data consisting of input points x and their corresponding output values u_h. The proposed hybrid method achieves its greatest efficiency by performing a single FEM analysis on a coarse mesh and incurring lower RBFNN training costs than complete mesh refinement. The model $\hat{u}(x)$ enables evaluations at any selected location, which makes it ideal for both parametric research and immediate simulation requirements. The RBFNN serves as a data-driven function approximator within the hybrid FEM–RBFNN framework, thereby improving the accuracy of FEM solutions. The theoretical foundation of the method depends on radial basis functions, which approximate functions and the system, thereby reducing errors through additive error reduction. The RBFNN creates a smooth and precise surrogate by learning from coarse-mesh FEM outputs, delivering faster PDE solution approximation than traditional mesh-refinement methods.

3.8 Computational Complexity and Efficiency Analysis

The computational complexity of the hybrid FEM-RBFNN model is determined by three processes: finite element discretisation and matrix assembly, and Radial Basis Function Neural Network training. The primary costs of FEM depend on the selected solver because they involve two tasks: stiffness matrix development that grows according to $\mathscr{O}(N)$ and linear system solving that ranges from $\mathscr{O}(n^{1.5})$ to $\mathscr{O}(n^3)$. Evaluating radial basis functions ($\mathscr{O}(n^2)$ and solving for weights ($\mathscr{O}(n^3)$ RBFNN introduces complexity.

Leveraging RBFNN for interpolation and refinement, the hybrid model enhances accuracy without undue FEM refinement. Particularly for complex geometries, this reduces computational costs while preserving accuracy. Although the worst-case complexity is $\mathscr{O}(N) + \mathscr{O}(n^3)$, solver and training modifications can improve efficiency and thereby make the method a feasible substitute for pure FEM for PDE solutions.

4 Results and Discussion

4.1 Experimental Settings

The problems considered are partial differential equations spanning both time-dependent and steady-state scenarios, accompanied by suitable boundary and initial conditions and known exact solutions for validation. A nonlinear Schrödinger Equation (NLSE) is defined over a one-dimensional spatial domain and typically involves time dependence. It is a dispersive partial differential equation where the nonlinearity arises from the interaction term, often of cubic type ($|\psi|^2\psi$). The NLSE is widely used to model phenomena such as wave propagation in nonlinear optical fibres, Bose–Einstein condensates, and deep-water waves. The solution to the NLSE often exhibits localised wave packets, known as solitons, which maintain their shape over time due to the balance between dispersion and nonlinearity. Boundary conditions may vary; periodic or homogeneous Dirichlet conditions are commonly used, and an initial condition specifies the initial wave profile. The problem serves as a benchmark in numerical analysis, but here the focus is on assessing schemes capable of handling nonlinearity, wave-like behaviour, and complex-valued solutions. Numerical methods must maintain essential physical properties, including mass and energy conservation throughout the entire time interval. The process serves as a fundamental test method which enables researchers to assess how well their time-stepping methods and spatial discretisation procedures function.

The study assesses two approaches, the Finite Element Method and the FEM-Radial Basis Function Neural Network, to solve three nonlinear partial differential equations which hold essential value for scientific and technical fields. The researchers applied multiple numerical methods, along with optimisation techniques, to improve stability and accuracy. The research team conducted systematic adjustments of key hyperparameters, including the gamma value, initial points (n-init), and RBF centres, to enhance model performance [15, 18]. The researchers used data from FEM to create their input for FEM-RBFNN after they completed the normalisation process, which resulted in better generalisation and convergence according to the findings of [1]. Google Colab served as the computational environment

for experiments because it handled the FEM and FEM-RBFNN computational requirements despite lacking high-performance computing optimisation. The implementation used Python as the main programming language, combining Matplotlib for visualisation with NumPy and SciPy for numerical computations, and Scikit-learn and PyTorch for neural network training [21, 22]. FEniCS provides an effective framework for solving PDEs through its finite element analysis system, which is based on [23]. The implementation of automated code-generation techniques improved efficiency for high-order FEM computations. The research demonstrates how hyperparameter optimisation, data standardisation, and FEM-RBFNN integration work with the study to show the advantages and weaknesses of the two methods, which will enable the creation of more effective numerical approaches for solving difficult differential equations [2, 16].

4.2 Numerical Examples

Consider this 1D nonlinear Schrodinger equation.[4]

$$i\frac{\partial \psi(x,t)}{\partial t} = -\frac{1}{2}\frac{\partial^2 \psi(x,t)}{\partial x^2} + |\psi(x,t)|^2\psi(x,t) \tag{23}$$

To solve this using the Finite Element Method, we decompose the complex wave function $\psi(x,t)$ into its real and imaginary components, u and v, respectively, such that $\psi = u + iv$. This yields a coupled system of real-valued partial differential equations:

$$\frac{\partial u}{\partial t} = -\frac{1}{2}\frac{\partial^2 v}{\partial x^2} - (u^2+v^2)v \tag{24}$$

$$\frac{\partial v}{\partial t} = \frac{1}{2}\frac{\partial^2 u}{\partial x^2} + (u^2+v^2)u \tag{25}$$

i: Imaginary unit, $\frac{\partial \psi}{\partial t}$: Time derivative (evolution), $\frac{\partial^2 \psi}{\partial x^2}$: Spatial second derivative (dispersion), $|\psi|^2\psi$: Cubic nonlinearity (self-interaction term).

1D nonlinear Schrödinger (NLSE) solution module $|\psi|$. The solution is generated with FEM and used as a reference solution. We also show the solution at different time frames $t = \pi, \frac{\pi}{8}, \frac{\pi}{4}, \frac{3\pi}{8}, \frac{\pi}{2}$.

The initial boundary value problem, given a domain $\Omega = [-10,10]\times(0,T]$, is written as:

$$\begin{cases} i\psi_t + 0.5\psi_{xx} + |\psi|^2\psi = 0 & (x,t)\in\Omega \\ \psi(0,x) = 2\,\mathrm{sech}(x) & x\in[-5,5] \\ \psi(t,-5) = \psi(t,5) & t\in(0,T] \\ \psi_x(t,-5) = \psi_x(t,5) & t\in(0,T] \end{cases} \tag{26}$$

where $T = \frac{\pi}{2}$.

The 1D Nonlinear Schrödinger Equation (NLSE) is a fundamental model in nonlinear optics and quantum mechanics. We consider the dimensionless form:

$$i\frac{\partial \psi}{\partial t} + \frac{1}{2}\frac{\partial^2 \psi}{\partial x^2} + |\psi|^2\psi = 0 \tag{27}$$

4.3 Temporal Discretisation: Semi-Implicit Crank-Nicolson

The Crank-Nicolson CN method provides second-order temporal accuracy and necessary numerical stability. The CN method approximates the solution at the midpoint $t_{n+1/2} = t_n + \Delta t/2$ using an arithmetic average of the values at the current and subsequent time steps. The semi-discrete equations for the coupled NLSE system are established through the following equations.

$$\frac{u^{n+1}-u^n}{\Delta t} = \mathscr{L}_u(u^{n+1/2}, v^{n+1/2}) \tag{28a}$$

$$\frac{v^{n+1}-v^n}{\Delta t} = \mathscr{L}_v(u^{n+1/2}, v^{n+1/2}) \tag{28b}$$

where $\phi^{n+1/2} = \frac{1}{2}(\phi^{n+1}+\phi^n)$. To avoid the computational overhead of solving a fully nonlinear system at each step, we implement a semi-implicit linearisation. The nonlinear potential $|\psi|^2$ is lagged by one half-step, evaluated at t_n:

$$|\psi^{n+1/2}|^2 \approx (u^n)^2 + (v^n)^2 \tag{29}$$

The corresponding variational (weak) form implemented in the FEniCS framework involves finding $\blacksquare = (u,v)\in\mathscr{V}$ such that:

$$\begin{aligned} \left\langle \frac{\blacksquare - \blacksquare^n}{\Delta t}, \phi \right\rangle + a\left(\blacksquare^{n+\frac{1}{2}}, \phi\right) \\ + c\left(\blacksquare^n; \blacksquare^{n+\frac{1}{2}}, \phi\right) = 0, \qquad \forall \phi \in \mathscr{V}. \end{aligned} \tag{30}$$

where $a(\cdot,\cdot)$ represents the linear dispersive terms and $c(\cdot;\cdot,\cdot)$ represents the linearised cubic interaction. This formulation preserves the Hamiltonian structure of the NLSE more effectively than explicit methods, preventing non-physical growth of the soliton amplitude over long integration times.

4.4 Ground Truth (Fine FEM) and FEM-RBFNN Strategy

The Ground Truth is established using a high-fidelity Finite Element mesh containing $N_{fine} = 800$ linear Lagrange elements. This resolution enables the system to detect the abrupt changes which occur during soliton phase transitions.

The surrogate modelling framework establishes a connection between two opposing requirements by providing fast computations which maintain precise numerical results.

Table 2 Performance Comparison at $t = \pi/4$

Method	L^2 Error	L_∞ Error	CPU Time (s)
FEM	0.012181	0.039490	1.4089
FEM-RBFNN	0.014309	0.057344	0.0760

The project aims to train a Radial Basis Function Neural Network to generate a precise solution estimate from data obtained from an economical coarse-grid simulation ($N_{coarse} = 100$). The Finite Element Method (FEM) uses a physics-based approach to solve problems, while neural networks can recover spatial details through interpolation.

The first phase, Data Generation, involves solving the coupled NLSE on the coarse mesh to obtain the discrete wave magnitude $|\psi_{coarse}(x,T)|$. The data collected from the coarse mesh exhibit inherent discretisation errors because its resolution fails to meet the Nyquist criterion required to capture fine-scale dispersive ripples. The RBFNN uses its localised basis functions to filter out the errors, which it treats as "noise."

In the training phase, the RBFNN uses spatial coordinates x to create the output magnitude $\hat{\psi}$. The network architecture consists of a hidden layer of M Gaussian kernels. To ensure the surrogate accurately represents the soliton peak, we employ K-Means clustering to define the kernel centres c_j. This unsupervised learning step clusters the centres around the spatial regions of highest data density. The final surrogate model is formulated as:

$$\hat{\psi}(x) = \sum_{i=1}^{M} w_j \exp\left(-\frac{|x-c_j|^2}{2\sigma^2}\right) \tag{31}$$

The weights w_j are determined by linear least-squares optimisation, which minimises the L_2 norm of the error relative to the coarse training samples. The resulting model provides a continuous, high-resolution reconstruction that can be evaluated at $N_{fine} = 800$ nodes at a fraction of the cost of a full fine-mesh simulation.

Based on the computational experiment, the performance metrics are summarised in Table 2.

The experimental results demonstrate the high efficiency of the RBFNN as a surrogate model for the NLSE. The primary findings are detailed below:

Computational Efficiency The RBFNN method provides its main benefit through its ability to decrease computational requirements. The Fine FEM process needs about 4.60 seconds to complete its final state but the RBFNN evaluation process finishes in only 0.076 seconds. The system achieves a performance increase of approximately **60x** when compared to actual measurements and the system achieves a performance increase of **18x** when compared to the training coarse solver.

Accuracy and Generalisation The RBFNN achieves an L_2 error of 0.0143 which approaches the approximate error of the coarse training data that measures 0.0122. The surrogate shows high accuracy in representing the main soliton peak. The coarse grid exhibits a L_∞ error increase to 0.057 which occurs at the dispersive tails of the wave. The Gaussian kernels improve numerical noise reduction of the coarse mesh yet they function as a low-pass filter which causes slight reduction in the peak frequency oscillations of the dispersive wave components.

4.5 Strengths and Limitations of the Proposed Method

By honing FEM solutions without requiring denser meshes, the FEM-RBFNN method improves accuracy and reduces computational costs. Its ability to interpolate helps reduce numerical oscillations and enhance generalisation, hence facilitating the handling of complicated geometries. Still, parameter selection is quite important, as poor choices can lead to instability or suboptimal approximations. Furthermore, even if FEM-RBFNN speeds up predictions, the initial RBFNN training adds significant computational overhead, especially when clustering with K-Means. As shown in situation 3, FEM alone was sufficient; thus, the usefulness of the hybrid model depends on the situation. FEM-RBFNN is most helpful when FEM suffers from accuracy issues. FEM-RBFNN provides, all things considered, a balanced and effective method for solving difficult PDEs, greatly enhancing numerical solutions while preserving computational feasibility.

5 Conclusion and Future Work

5.1 Summary of Findings

This study successfully implemented a hybrid FEM-RBFNN framework to optimise the numerical simulation of the Nonlinear Schrödinger Equation (NLSE). While the Finite Element Method (FEM) provides a robust mathematical foundation for managing complex wave dynamics, high-fidelity simulations on fine meshes are often computationally prohibitive. By integrating Radial Basis Function Neural Networks (RBFNNs), this work established an efficient surrogate model capable of reconstructing high-resolution wave profiles from computationally "cheap" coarse-grid data.

The benchmark tests showed that the soliton propagation testing demonstrated that the FEM-RBFNN method achieved a complete transformation of computational requirements for its calculations. The surrogate model achieved a speed improvement of 60 times, as indicated by the quantitative results, which showed it performed at

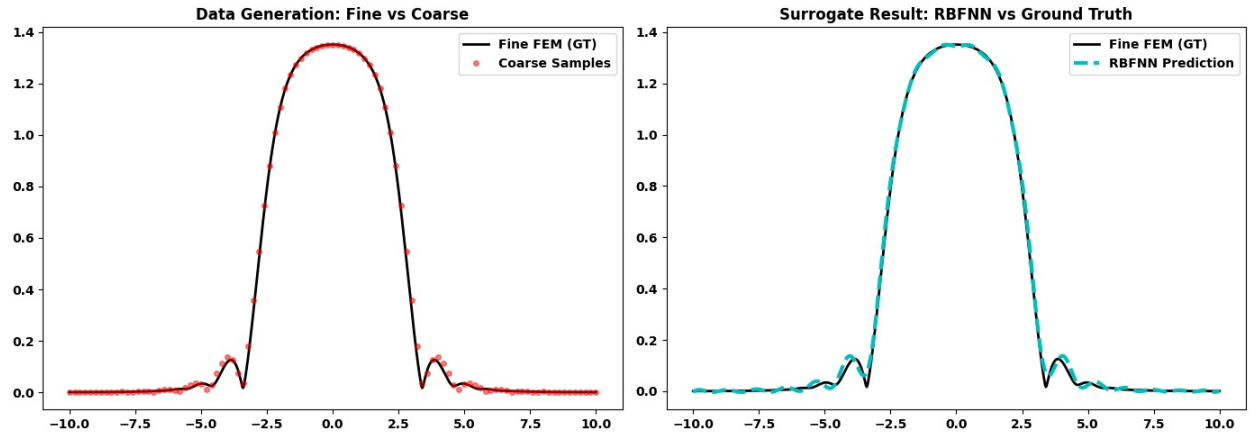

Fig. 2 Comparison of numerical solutions: (Left) Generation of training data via coarse sampling against the ground truth; (Right) RBFNN prediction vs. Fine FEM ground truth.

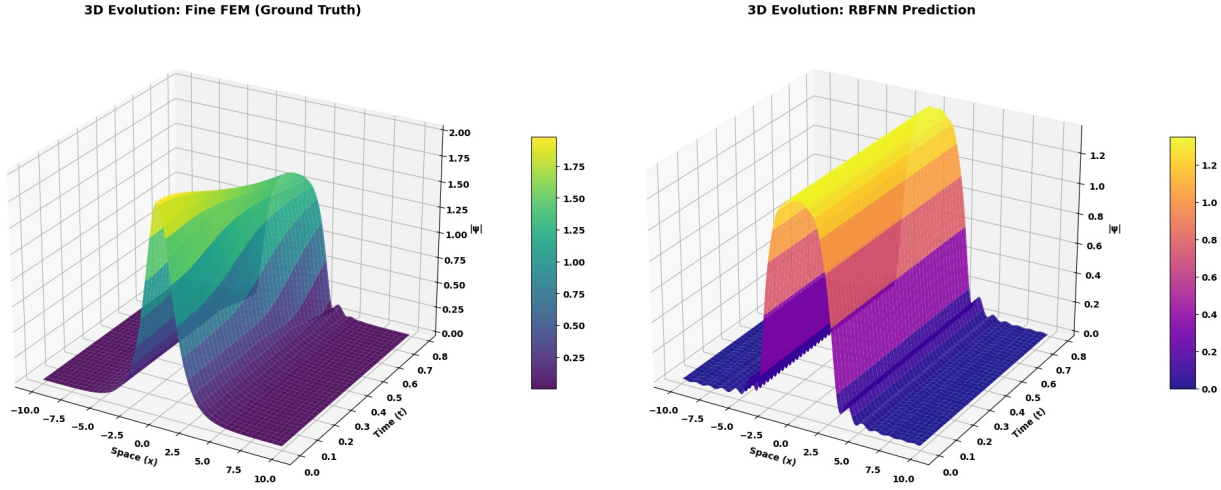

Fig. 3 Side-by-side 3D comparison of wave magnitude evolution. The left panel displays the Fine FEM (Ground Truth), while the right panel displays the RBFNN Prediction. The RBFNN successfully captures the qualitative features of the soliton's propagation. However, as seen in the right panel, the RBFNN tends to act as a low-pass filter, slightly smoothing the dispersive ripples found at the base of the soliton peak. This is an expected characteristic of Gaussian RBF kernels when the centre density M is lower than the Nyquist frequency of the underlying mesh.

0.08 seconds for the fine-mesh ground truth, compared to 4.60 seconds for the coarse-mesh ground truth. The RBFNN model produced an L_2 error of approximately 0.014, which closely matched the actual discretisation error of the coarse training data, 0.012. The results demonstrate that RBFNNs can use K-Means clustering to select their optimal centres, which serve as continuous interpolators that eliminate numerical artefacts arising from coarse FEM distributions.

The RBFNN system preserves the coarse training set discretisation boundaries while providing users with a rapid differentiable model that displays wave amplitude. The hybrid method provides an effective and promising solution that enables researchers to conduct real-time wave analysis and study multiple parameters at large scales, whereas the standard FEM fine-mesh approach requires an unfeasible computational budget.

The FEM-RBFNN system requires more work on automated hyperparameter tuning for the RBF shape parameter ε. The proposed strategy provides a direct pathway to high-accuracy numerical results that require fewer computational resources.

The FEM-RBFNN surrogate system provides reliable speed and accuracy, making it suitable for real-time wave-propagation analysis and large parameter sweeps that exceed the limits of full FEM simulations.

5.2 Contributions to Knowledge

The research project demonstrates how numerical analysis advances through the successful application of the Finite Element Method (FEM) and Radial Basis Function Neural Networks (RBFNNs), which serve as fast surrogates

for modelling nonlinear wave behaviour. The study demonstrates that RBFNNs can serve as "super-resolution" interpolators, recreating the complete soliton profile using limited common grid information.

The work achieves its primary goal by reducing computational requirements. The semi-implicit Crank-Nicolson FEM method produced training data that enabled the hybrid model to achieve a 60x speedup while keeping the Nonlinear Schrödinger Equation (NLSE) solution unaffected. The study demonstrates that K-Means clustering improves RBF centre placement by enabling the neural network to correctly identify location-based events, including soliton peaks. This method provides executives with a fixed system that combines established deterministic solvers with machine learning systems to address the nonlinear physics requirements for both spatial and temporal resolution.

5.3 Future Research Directions

The research must advance by extending the existing framework to provide complete time-dependent surrogates that can use Recurrent Neural Networks (RNNs) and Long Short-Term Memory (LSTM) networks to model the future evolution of $|\psi|$ over all future time periods without rerunning the FEM solver. The engineering value of the hybrid model should increase through its extension to higher-dimensional PDEs, including 2D and 3D NLSE systems for research on optical filamentation and multi-physics fluid dynamics.

The RBFNN evaluation should use GPU-accelerated systems, as this implementation will enhance the efficiency of real-time wavefront sensing during control processes. Research into automated hyperparameter optimisation must be conducted to test the RBF shape parameter ε and the number of centres M across various initial conditions. The FEM-RBFNN framework should be used for industrial-scale simulations in structural analysis, heat transfer, and electromagnetics to test its ability to serve as a general scientific computing tool in hybrid scientific computing.

References

1. A. Sacchetti, et al. (2011). Neural networks to solve partial differential equations: A comparison with finite elements.
2. M. O. Ogunniran, et al. (2024). Enhanced rational multi-derivative integrator for singular problems with applications to advection equations. *Ain Shams Engineering Journal*.
3. F. Mostajeran and S. M. Hosseini (2023). Radial basis function neural network (RBFNN) approximation of Cauchy inverse problems. *Computers & Mathematics with Applications*, 141, 129–144. DOI: 10.1016/j.camwa.2023.04.026
4. S. Cuomo, et al. (2022). Scientific machine learning through physics-informed neural networks: Where we are and what's next. *arXiv*. https://arxiv.org/abs/2201.05624
5. C. Uriarte (2023). Solving partial differential equations using artificial neural networks (Doctoral dissertation, University of the Basque Country). Retrieved from https://addi.ehu.es/handle/10810/68335
6. W. K. Liu, S. Li, and H. S. Park (2022). Eighty years of the finite element method: Birth, evolution, and future. *Archives of Computational Methods in Engineering*, 29, 4431–4453. DOI: 10.1007/s11831-022-09740-9
7. J. P. Narain (2021). Comparison of neural network and finite difference solutions. *American Journal of Computational and Applied Mathematics*, 11(3), 65–70.
8. P. B. Zhou (1993). Finite difference method. In *Numerical Analysis of Electromagnetic Fields*. Springer.
9. D. Komatitsch and J. Tromp (1999). Introduction to the spectral element method for three-dimensional seismic wave propagation. *Geophysical Journal International*, 139(3), 806–822. DOI: 10.1046/j.1365-246X.1999.00967.x
10. H. Chen, L. Kong, and W.-J. Leng (2010). Numerical solution of PDEs via integrated radial basis function networks with adaptive training algorithm.
11. I. Babuska and W. C. Rheinboldt (1978). Error estimates for adaptive finite element computations. *SIAM Journal on Numerical Analysis*, 15(4), 736–754. DOI: 10.1137/0715049
12. G. Cybenko (1989). Approximation by superpositions of a sigmoidal function. *Mathematics of Control, Signals and Systems*, 2(4), 303–314. DOI: 10.1007/BF02551274
13. S. Hochreiter and J. Schmidhuber (1997). Long short-term memory. *Neural Computation*, 9(8), 1735–1780. DOI: 10.1162/neco.1997.9.8.1735
14. G. Bebis and M. Georgiopoulos (1994). Feed-forward neural networks. *IEEE Potentials*, 13(4), 27–31. DOI: 10.1109/45.329294
15. S. Chen, C. F. N. Cowan, and P. M. Grant (1991). Orthogonal least squares learning algorithm for radial basis function networks. *IEEE Transactions on Neural Networks*, 2(2), 302–309. DOI: 10.1109/72.80341
16. J. Berg and K. Nyström (2018). Neural network augmented inverse problems for PDEs. Department of Mathematics, Uppsala University.
17. S. Emmanuel, S. Sathasivam, and M. O. Ogunniran (2024). Multi-derivative hybrid block methods for singular initial value problems. *Scientific African*, 24, e02141.

18. S. K. Mitusch, S. W. Funke, and M. Kuchta (2021). Hybrid FEM-NN models: Combining artificial neural networks with the finite element method. Simula Research Laboratory.
19. S. Emmanuel, S. Sathasivam, and M. O. Ogunniran (2024). Leveraging feed-forward neural networks to enhance the hybrid block derivative methods. *Journal of Computational Mathematics and Data Science*, 13, 100101.
20. M. O. Ogunniran, et al. (2025). Harnessing neural networks in hybrid block integrator for efficient solution of boundary value problems. *Thermal Advances*, 2, 100022.
21. M. Abadi (2015). TensorFlow.org. Retrieved from https://www.tensorflow.org
22. A. Paszke, et al. (2019). PyTorch: An imperative style, high-performance deep learning library. In *Proceedings of NeurIPS 2019* (pp. 1–12).
23. A. Logg (2016). Mesh generation in FEniCS. Retrieved from http://www.logg.org/anders/2016/generation-in-fenics

TTMP vol 3 (2), 2026
doi: 10.30511/TTMP.2026.2089573.1078

Transactions in Theoretical and Mathematical Physics

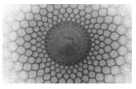

Metastable de Sitter Vacua from Critical Scalar Theory

Ehsan Bavarsad[1], **Farhang Loran**[a2]

[1]Department of Physics, University of Kashan, 8731753153 Kashan, Iran
[2]Department of Physics, Isfahan University of Technology, Isfahan 84156-83111, Iran

Received: 24 April 2026 / Accepted: 05 May 2026 / Published: 09 May 2026

Abstract Studying the critical scalar theory in four dimensional Euclidean space with the potential term $-g\phi^4$ we show that the theory can not be analytically continued through $g = 0$ from $g < 0$ region to $g > 0$ region. For $g > 0$ although energy is not bounded from below but there exist a classical trajectory with an AdS_5 moduli space, corresponding to a metastable local minima of the action. The fluctuation around this solution is governed by a minimally coupled scalar theory on four dimensional de Sitter background with a reversed Mexican hat potential. Since in the weak coupling limit, the partition function picks up contribution only around classical solutions, one can assume that our de Sitter universe corresponds to that local minima which lifetime increases exponentially as the coupling constant tends to zero. Similar results is obtained in the case of critical scalar theory coupled to U(1) gauge field which is essential for people living on flat Euclidean space to observe a de Sitter background by optical instruments.

Keywords: critical scalar theory; de Sitter vacua

1 Introduction

Recently, we showed that the fluctuations of the scalar field around the classical trajectory of massless ϕ^4 model in four dimensional flat Euclidean spacetime is governed by a conformally coupled scalar field theory in four dimensional de Sitter background [1]. This result is interesting due to its uniqueness. In four dimensions, in principle, one can consider two classes of critical (classically scale-free) scalar field theories i.e. massless ϕ^4 models on Euclidean (Minkowski) spacetime with g, the coupling constant, either positive or negative (we assume the potential $V(\phi) = -\frac{g}{4}\phi^4$). Although scalar theory with $g > 0$ seems to be not physical as energy is not bounded from below but as is shown in [1] in this case, the Euler-Lagrange equation of motion of the scalar theory on Euclidean space has an interesting classical solution say ϕ_0 with finite action $S[\phi_0] \sim g^{-1}$. Interestingly, as far as we are considering real scalar field theories the model with the physical potential i.e. the case of $g < 0$ has not such a solution, see Eq.(1). We should clarify that from our previous viewpoint [1], for $g < 0$, one can still consider a solution like ϕ_0 obtained by an analytic continuation from $g > 0$ to $g < 0$ region. But such a solution is singular on the surface of a sphere which radius is proportional to g. Consequently the action $S[\phi_0]$ is infinite and ϕ_0 can not be considered as a classical trajectory. If one ignores this problem and follows the calculations one obtains a conformally coupled scalar field on AdS_4 background. The reason why we do not follow our previous point of view turns back to our new machinery for constructing ϕ_0 from the first principles explained in section 2. Of course similar singularities appear even for $g > 0$, when one switches to Minkowski spacetime by Wick rotation $x^0 \to ix^0$. But in this case ($g > 0$) one can argue that the singularity is beyond the horizon of observers living in the corresponding de Sitter spacetime and consequently is safe. We do not study the case of Minkowski spacetime in this paper.

As is shown in [1] the information geometry of the moduli of ϕ_0 is AdS_5 (dS_5) if $g > 0$ ($g < 0$) which resembles the information geometry of $k = 1$ $SU(2)$ instantons [2] [1]. The moduli here are the location of the center of ϕ_0 and its size and are consequences of the invariance of the action under rescaling and translation. The similarity between this solution and SU(2) instantons can be explained in terms of the 't Hooft ϕ^4 ansatz for instantons [3].

[a]loran@iut.ac.ir

[1] $V(\phi_0)$ can be shown to be proportional to the SU(2) one-instanton density [2].

In this paper focusing on the case $g > 0$ we show that ϕ_0 can be responsible for viewing a metastable de Sitter background. We first show that ϕ_0 is a metastable local minima of the action. Then we show that the weak coupling limit $g \to {}^+0$ is equivalent to the classical ($\bar{h} \to 0$) limit therefore in that limit the partition function picks up contribution only around the classical trajectory ϕ_0. As we said before, fluctuations around ϕ_0 is governed by a scalar theory on a de Sitter background with a reversed Mexican potential. The hight and width of the barrier is proportional to R and g^{-1}. Here R is the scalar curvature of the universe which can not be determined in our model but one can show that the lifetime of this local minima is proportional to $e^{g^{-1}}$.

Summarizing these results we verify that the critical scalar theory can not be analytically continued (at least through $g = 0$) from $g < 0$ region to $g > 0$ region. These results are strictly important from perturbation theory point of view. In the $g \to {}^-0$ limit, valid perturbations are around $\phi = 0$ in a *flat* Euclidean background but in the $g \to {}^+0$ limit perturbations are around $\phi = 0$ in an Euclidean *de Sitter* background. More explicitly at $g = 0^-$, the theory is simply a free massless scalar theory on flat Euclidean space but at $g = 0^+$ due to $\bar{h}$ considerations the theory is a (free and stable) conformally coupled scalar theory on an Euclidean de Sitter background. See sections 2 and 3.

But why we are interested in de Sitter background. In fact WMAP results [4] combined with earlier cosmological observations shows that we are living in an accelerating universe. Constructing four dimensional de Sitter vacuum as a string theory (M-theory) solution has been a long standing challenge. In [5] KKLT constructed a metastable de Sitter vacua of type IIB string theory by adding $\overline{\text{D3}}$-branes to the GKP [6] model of highly warped IIB compactifications with nontrivial NS and RR three-form fluxes. The mean lifetime of KKLT solution is $10^{10^{120}}$ years. KKLMMT constructed a model of inflation by adding mobile D3 branes to the KKLT solution [7]. In such models the inflaton (the position of D3 brane deep inside the warped throat geometry) is a conformally coupled scalar in the effective four-dimensional geometry. Therefore the mass of such a scalar m_ϕ^2 is close to $2H^2 = \xi R$ where H^2 is the Hubble parameter, $\xi = \frac{1}{6}$ (in four dimension) is the conformal coupling constant and R is the curvature of de Sitter space. As is uncovered in [7] this does not meet the observational requirement $m_\phi^2 \sim 10^{-2} H^2$ [2]. Similar considerations show that our model can not be a successful model for inflation since in the $g \to {}^+0$ limit we also obtain a conformally coupled scalar theory on de Sitter background.

[2] In D3/D7 model of inflation one does not encounter the $m_\phi^2 \sim H^2$ problem. But here in contrast to the model of D3/$\overline{\text{D3}}$ inflation in the highly warped throat, there is no natural mechanism for suppressing the contribution of cosmic strings formed at the end of inflation to the CMB anisotropy. See [8] for a solution to this problem.

Another problem in our model is the existence of a continuum of de Sitter bubbles, given by the location of the center of ϕ_0 and its size. Naively this number is proportional to the volume of the AdS_5 moduli space. If ϕ_0 is responsible to observe, say, by *optical* methods a de Sitter geometry (see section 4), a natural question is to ask which bubble we live in. Studying the variation of action around the ϕ_0 solution, we have verified, by numerical calculations that smaller bubbles are more stable than larger ones. Consequently there is a transition: larger bubbles decay to smaller ones and probably finally there remains a gas of zero size bubbles. The mechanism of such a decays is not clear to us yet but its phenomenology, might be similar to that of the discretuum of possible de Sitter vacua in KKLT models [9].

As we said before our theory can not do any prediction about the size of our de Sitter universe or the nature of the scalar field but it predicts that the lifetime of this metastable vacua is $\tau \sim e^{g^{-1}}$. The model is interesting due to its uniqueness and symmetries which brings hopes to be constructible from a fundamental theory like string theory.

The organization of the paper is as follows. In section 2, we study the critical scalar theory in $D = 4$ Euclidean space and ϕ_0, the exact solution to the corresponding Euler-Lagrange equation of motion. Considering the weak coupling limit we show that the partition function only picks up contribution around ϕ_0. In section 3, we show that the critical scalar theory considered as the action for (not essentially small) fluctuations around ϕ_0 is a scalar theory on $D = 4$ de Sitter background. Consequently we verify that in the weak coupling limit the critical scalar theory of section 2is in fact a metastable scalar theory on de Sitter background with finite lifetime increasing exponentially as the coupling constant decreases. In section 4 we generalize our model to scalar theory coupled to U(1) gauge field. Such a generalization is essential as it shows how by optical observations people living in a flat Euclidean space can view a de Sitter geometry for their universe.

2 Critical scalar theory in $D = 4$ Euclidean space

In this section we study scalar field theories in four dimensional Euclidean space invariant under rescaling transformation. By rescaling we mean a coordinate transformation $x \to x' = \lambda x$, $\lambda > 0$. Requiring the kinetic term of a scalar theory to be invariant under rescaling, one verifies that the scalar field should be transformed as $\phi(x) \to \phi'(x') = \lambda^{-1}\phi(x)$. A scale free theory by definition is a theory given by an action S invariant under rescaling. In addition to the Kinetic term which variation is a total derivative, we search for polynomials $V(\phi)$ in ϕ as the potential term such that $\delta V = 0$, up to total derivatives. Such polynomials exist only in three, four and six dimensions. In the case of our interest i.e. $D = 4$,

$V(\phi) = \frac{-g}{4}\phi^4$. Here g, the coupling constant is some arbitrary real constant which is by construction invariant under rescaling. Such a scalar model is called critical as it is scale-free and its correlation length is infinite. The corresponding Euler-Lagrange equation of motion is a nonlinear Laplace equation $\nabla^2\phi + g\phi^3 = 0$. One can easily show that for $g > 0$, a solution of the non-linear Laplace equation is [1, 9],

$$\phi_0(x;\beta,a^\mu) = \sqrt{\frac{8}{g}}\frac{\beta}{\beta^2+(x-a)^2}, \tag{1}$$

where $(x-a)^2 = \delta_{\mu\nu}(x-a)^\mu(x-a)^\nu$. β and a^μ are undetermined parameters describing the the size and location of ϕ_0. These moduli are consequences of symmetries of the action i.e. invariance under rescaling and translation. The information geometry of the moduli space, given by Hitchin formula [10]

$$\mathscr{G}_{IJ} = \frac{1}{N}\int d^4x\mathscr{L}_0\partial_I(\log\mathscr{L}_0)\,\partial_J(\log\mathscr{L}_0), \tag{2}$$

is an Euclidean AdS$_5$ space [1],

$$\mathscr{G}_{IJ}d\theta^I d\theta^J = \frac{1}{\beta^2}\left(d\beta^2 + da^2\right). \tag{3}$$

$I = 1,\cdots,5$ counts space directions of moduli space $\theta^I \in \{\beta, a^\mu\}$, $N = \frac{4^3}{5}\int d^4x\mathscr{L}_0$ is a normalization constant and $\mathscr{L}_0 = \frac{g}{4}\phi_0^4$ is the Lagrangian density calculated at $\phi = \phi_0$. The moduli a^μ are present since the action is invariant under transformation. The existence of β is the result of invariance under rescaling. To see this let us consider scale-free fields i.e. those fields that satisfy the relation $\delta_\varepsilon\phi = 0$. Here $\delta_\varepsilon\phi(x) = \phi'(x) - \phi(x)$ is the infinitesimal scale transformation given by $\lambda = 1+\varepsilon$ for some infinitesimal ε. To this aim we first note that rescaling leaves the origin ($x = 0$) invariant. Consequently $\phi(0)$ is distinguished from the values of the field at the other points since $\phi(0) \to \phi'(0) = \lambda^{-1}\phi(0)$. Therefore, it is plausible to make the dependence of scalar fields on their values at the origin explicit and represent the rescaling transformation by $\phi(x;\phi(0)) \to \phi'(x;\phi(0)) = \lambda^{-1}\phi(\lambda^{-1}x;\lambda\phi(0))$. Defining $\beta^{-1} = \phi(0)$, one can show that $\delta_\varepsilon\phi(x) = -\varepsilon(1+x^I\partial_I)\phi(x)$, where $x^I \in \{x^\mu,\beta\}$. The $SO(4)$ invariant solutions of equation $\delta_\varepsilon\phi = 0$ satisfying the condition $\phi(0;\phi(0)) = \phi(0)$ are $\phi_k = c\beta^{-1}\left(\frac{\beta}{\sqrt{\beta^2+x^2}}\right)^{k+2}$ where c is some arbitrary constant. It is easy to see that for $c = \sqrt{\frac{8}{g}}$, ϕ_0, among the others, is the solution of classical equation of motion.

Now it is time to show that ϕ_0 is a metastable local minima of the action. Since ϕ_0 is a solution of Euler-Lagrange equation of motion $\delta S = 0$ it is a local extremum of the action[3]. So it is enough to show that there are field variations $\phi_0 \to \phi_\eta = \phi_0 + \varepsilon\eta$ for $\mathscr{C}^1$ functions η vanishing as $x \to \infty$ such that $\delta S = c_\eta\varepsilon^2 + \mathscr{O}(\varepsilon^3)$ for some real positive constant c_η. For simplicity one can assume $\eta = \left(\frac{1}{1+x^2}\right)^n$, $g = 8$, $b = 1$ and calculate $\delta S = S[\phi_\eta] - S[\phi_0]$ for some integers n. One recognizes that $c_n > 0$ for $n > 5$, though it is negative for $0 < n \leq 5$. A good sign for metastability of the action at ϕ_0. Section 3 provides an exact proof for this claim. Another interesting observation is that bubbles with larger size are less stable than those with smaller size. This can be checked noting that the size of a bubble is proportional to β^{-1}. By repeating the above calculations one easily verifies that for example for $b = 3$ $c_n > 0$ even for $n = 3$. Unfortunately without analytic data all these observations make only a rough picture of the phenomena which can not be used to make an exact statement.

The weak coupling limit

To study the weak coupling limit of the theory one can scale $g \to \frac{g}{\lambda^2}$ and consider the $\lambda \to \infty$ limit, while keeping fields ϕ undistorted. To this aim we do the following transformations,

$$\begin{array}{lll} x \to \lambda x, & & x \to x, \\ \phi \to \lambda^{-1}\phi, & \text{and} & \phi \to \lambda\phi, \\ g \to g, & & g \to \lambda^{-2}g, \end{array} \tag{4}$$

which results in the desired transformation:

$$\begin{array}{l} x \to \lambda x, \\ \phi \to \phi, \\ g \to \lambda^{-2}g, \\ S \to \lambda^2 S, \end{array} \tag{5}$$

More explicitly due to invariance under rescaling we have,

$$\int D[\phi]\, e^{-\frac{1}{\hbar}S[\phi;\lambda^{-2}g]} = \int D[\phi]\, e^{-\frac{\lambda^2}{\hbar}S[\phi,g]}. \tag{6}$$

To calculate the partition function one can instead of the transformation $S \to \lambda^2 S$ assume that $S \to S$ but $\bar{h} \to \lambda^{-2}\bar{h}$.

Consequently the $g \to {}^+0$ limit is equivalent to $\bar{h} \to {}^+0$ limit [4]. Therefore in the weak coupling limit the partition function picks up contribution only from trajectories close to ϕ_0. This key observation when we study coupling to $U(1)$ gauge field proves why people living in a flat Euclidean space with a critical scalar field at $g = 0^+$ observe a de Sitter universe.

[3] Of course from $\delta S = 0$ we can only conclude that ϕ_0 is a stationary point and not necessarily a local extremum. We continue by assuming that ϕ_0 is a local extremum. This assumption can be proved following the results of section 3.

[4] Of course we are also blowing our universe as $x \to \lambda x$. Since the flat Euclidean space we considered is not compact it does not seems to cause any problem at this level. In the case n-point functions one should note that non-coincident points go to infinity with respect to each other

3 ϕ_0 as a de Sitter background

In this section we show that fluctuations around ϕ_0 are governed by a scalar theory on de Sitter background. This section is a review of the calculations made in [1]. In order to study the fluctuations around ϕ_0 one should rewrite the action

$$S[\phi] = \int d^4x \left(\frac{1}{2}\delta^{\mu\nu}\partial_\mu\phi\partial_\nu\phi - \frac{g}{4}\phi^4 \right), \tag{7}$$

in terms of new fields $\tilde{\phi} = \phi - \phi_0$. In this way one obtains a new action,

$$S[\phi] = S[\phi_0] + S_{\text{free}}[\tilde{\phi}] + S_{\text{int}}[\tilde{\phi}], \tag{8}$$

where $S[\phi_0] = \int d^4x \mathscr{L}_0 = \frac{8\pi^2}{3g}$, and

$$S_{\text{free}}[\tilde{\phi}] = \int d^4x \left(\frac{1}{2}\delta^{\mu\nu}\partial_\mu\tilde{\phi}\partial_\nu\tilde{\phi} + \frac{1}{2}M^2(x)\tilde{\phi}^2 \right), \tag{9}$$

in which,

$$M^2(x) = -3g\phi_0^2 = -24\frac{\beta^2}{(\beta^2+(x-a)^2)^2}. \tag{10}$$

The mass dependent term can be interpreted as interaction with ϕ_0 background. Now recall that in general, by inserting $\tilde{\phi} = \sqrt{\Omega}\bar{\phi}$ and $\delta_{\mu\nu} = \Omega^{-1}g_{\mu\nu}$ in the action $S[\tilde{\phi}] = \int d^4x \frac{1}{2}\delta^{\mu\nu}\partial_\mu\tilde{\phi}\partial_\nu\tilde{\phi}$, one obtains,

$$S[\tilde{\phi}] = \int d^4x\sqrt{g} \left(\frac{1}{2}g^{\mu\nu}\partial_\mu\bar{\phi}\partial_\nu\bar{\phi} + \frac{1}{2}\xi R\bar{\phi}^2 \right), \tag{11}$$

i.e. a scalar theory on conformally flat background given by the metric $g_{\mu\nu}$ in which $\Omega > 0$ is an arbitrary $\mathscr{C}^\infty$ function. R is the scalar curvature of the background and $\xi = \frac{1}{6}$ is the conformal coupling constant. For details see [11] or appendix C of [1]. Thus, defining $\bar{\phi} = \Omega^{\frac{-1}{2}}\tilde{\phi}$, one can show that $S_{\text{free}}[\tilde{\phi}]$ given in Eq.(9) is the action of the scalar field $\bar{\phi}$ on some conformally flat background with metric $g_{\mu\nu} = \Omega\delta_{\mu\nu}$:

$$S_{\text{free}}[\tilde{\phi}] = \int d^4x\sqrt{|g|} \left(\frac{1}{2}g^{\mu\nu}\partial_\mu\bar{\phi}\,\partial_\nu\bar{\phi} + \frac{1}{2}(\xi R + m^2)\bar{\phi}^2 \right). \tag{12}$$

Here, $m^2\Omega = M^2(x)$, where m^2 is the mass of $\bar{\phi}$ (undetermined) and $M^2(x)$ is given in Eq.(10). This result is surprising as one can show that the Ricci tensor $R_{\mu\nu} = \Lambda g_{\mu\nu}$, where $\Lambda = -\frac{m^2}{2} > 0$ as far as $\Omega > 0$. Consequently $\bar{\phi}$ lives in a four dimensional de Sitter space which scalar curvature $R = -2m^2$. The interacting part of the action, $S_{\text{int}}[\tilde{\phi}] = \int d^4x\sqrt{|g_{\mu\nu}|}\mathscr{L}_{\text{int}}$ is well-defined in terms of $\bar{\phi}$ on the corresponding dS_4:

$$\mathscr{L}_{\text{int}} = -g\sqrt{\frac{-m^2}{3g}}\bar{\phi}^3 - \frac{g}{4}\bar{\phi}^4. \tag{13}$$

Interestingly after a shift of the scalar field $\bar{\phi} \to \bar{\phi} - \sqrt{\frac{-m^2}{3g}}$ the action (8) can be written in the dS_4 as follows:

$$S[\bar{\phi}] = \int d^Dx\sqrt{|g|} \left(\frac{1}{2}g^{\mu\nu}\partial_\mu\bar{\phi}\,\partial_\nu\bar{\phi} + \frac{1}{2}\xi R\bar{\phi}^2 - \frac{g}{4}\bar{\phi}^4 \right). \tag{14}$$

This is a scalar theory in a de Sitter background with reversed Mexican hat potential. $\bar{\phi} = 0$ corresponds to the local minima of the potential which distance to the center of the hill (the location of ϕ_0) is $\sqrt{\frac{\xi R}{g}}$. The hight of the hill is $\frac{\xi^2R^2}{4g}$. The lifetime of the metastable vacua can be estimated using the WKB method: the transition rate Γ is

$$\log\Gamma \sim -\Delta S, \qquad \Delta S \sim V_4\frac{(\xi R)^2}{g} \tag{15}$$

in which $V_4 \sim R^{-2}$ is the volume of the $\mathscr{S}^4$, the Euclidean de Sitter space. Consequently the lifetime $\tau \sim e^{g^{-1}}$.

4 Critical scalar theory coupled to $U(1)$ gauge field

In this section we study complex critical scalar theory on Euclidean space coupled to $U(1)$ gauge field A_μ,

$$S = \int d^4x \left(|D_\mu\phi|^2 - \frac{g}{2}|\phi|^4 \right) + S_A, \tag{16}$$

where $D_\mu = \partial_\mu + ieA_\mu$ is the covariant derivative and $S_A = -\frac{1}{4}F_{\mu\nu}F_{\rho\sigma}\delta^{\rho\mu}\delta^{\sigma\nu}$. It is easy to verify that $A_\mu = 0$ and $\phi = \phi_0$ is a solution of the Euler-Lagrange equation of motion. Inserting $\tilde{\phi} = \phi - \phi_0$ in the Eq.(16), one obtains

$$S = S[\phi_0] + \tilde{S}[\tilde{\phi}] + S_{int} + S_A, \tag{17}$$

where

$$S_{int} = \int d^4x\delta^{\mu\nu}\left[(ieA_\mu(\tilde{\phi}+\phi_0)\partial_\nu(\tilde{\phi}^*+\phi_0) + c.c.) + e^2A_\mu A_\nu|\tilde{\phi}+\phi_0|^2 \right], \tag{18}$$

$$\tilde{S}[\tilde{\phi}] = \int d^4x \left(\frac{1}{2}|\partial_\mu(\tilde{\phi}+\phi_0)|^2 - \frac{g}{4}|\tilde{\phi}+\phi_0|^4 \right). \tag{19}$$

Inserting $\bar{\phi} = \Omega^{-\frac{1}{2}}\tilde{\phi}$ where Ω is defined as before by the relation $\phi_0 = \sqrt{\frac{-m^2}{3g}}\Omega$ one obtains,

$$S_{int} = \int d^4x \frac{1}{2}\Omega\delta^{\mu\nu}\left[ieA_\mu\left(\bar{\phi} + \sqrt{\frac{-m^2}{3g}}\right)\partial_\nu\bar{\phi}^* + c.c. + e^2A_\mu A_\nu\left|\bar{\phi} + \sqrt{\frac{-m^2}{3g}}\right|^2\right], \tag{20}$$

and

$$\tilde{S}[\tilde{\phi}] = \int d^4x\left(\frac{1}{2}\Omega\left|\partial_\mu\bar{\phi}\right|^2 - \frac{g}{4}\left|\bar{\phi} + \sqrt{\frac{-m^2}{3g}}\right|^4 - \frac{1}{2}\sqrt{\Omega}\nabla^2\sqrt{\Omega}\left|\bar{\phi} + \sqrt{\frac{-m^2}{3g}}\right|^2\right), \tag{21}$$

where $\nabla^2 = \delta^{\mu\nu}\partial_\mu\partial_\nu$. Defining $g_{\mu\nu} = \Omega\delta_{\mu\nu}$ and noting that $-\sqrt{\Omega}\nabla^2\sqrt{\Omega} = \sqrt{g}\xi R$, after an obvious shift $\bar{\phi} \to \bar{\phi} - \sqrt{\frac{-m^2}{3g}}$, one obtains,

$$S = \int d^4x\sqrt{g}\left(\frac{1}{2}g^{\mu\nu}D_\mu\bar{\phi}D_\nu\bar{\phi}^* + \frac{1}{2}\xi R\left|\bar{\phi}\right|^2 - \frac{g}{4}\left|\bar{\phi}\right|^4\right) + S_A, \tag{22}$$

It is known that in $D = 4$, S_A is invariant under conformal transformation $\delta_{\mu\nu} \to \Omega\delta_{\mu\nu}$ and $A_\mu \to A_\mu$ thus one can write the action S_A equivalently as follows,

$$S_A = -\frac{1}{4}\int d^4x\sqrt{g}g^{\mu\rho}g^{\nu\sigma}F_{\mu\nu}F_{\rho\sigma}, \tag{23}$$

where $F_{\mu\nu} = \partial_\mu A_\nu - \partial_\nu A_\mu$ is the field strength in the de Sitter background. Consequently at $g = 0^+$ the theory given by the action (16) is a conformally coupled scalar theory minimally coupled to $U(1)$ gauge field on de Sitter background. Therefore at $g = 0^+$ using optical instruments people living on flat Euclidean space observe an accelerating universe.

References

1. F. Loran, "Nonlinear Laplace equation, de Sitter vacua, and information geometry," *Phys. Rev. D* **71** (2005), 126003. DOI: 10.1103/PhysRevD.71.126003, arXiv: hep-th/0501189.
2. M. Blau, K. S. Narain and G. Thompson, "Instantons, the Information Metric, and the AdS/CFT Correspondence," arXiv: hep-th/0108122.
3. G. 't Hooft, "Symmetry breaking through Bell-Jackiw anomalies," *Phys. Rev. Lett.* **37** (1976), 8–11. DOI: 10.1103/PhysRevLett.37.8; G. 't Hooft, "Computation of the quantum effects due to a four-dimensional pseudoparticle," *Phys. Rev. D* **14** (1976), 3432–3450. DOI: 10.1103/PhysRevD.14.3432; A. Actor, "Classical solutions of SU(2) Yang-Mills theories," *Rev. Mod. Phys.* **51** (1979), 461–525. DOI: 10.1103/RevModPhys.51.461.
4. D. N. Spergel et al., "First-Year Wilkinson Microwave Anisotropy Probe (WMAP) Observations: Determination of Cosmological Parameters," *Astrophys. J. Suppl.* **148** (2003), 175–194. DOI: 10.1086/377226, arXiv: astro-ph/0302209.
5. S. Kachru, R. Kallosh, A. Linde and S. P. Trivedi, "de Sitter vacua in string theory," *Phys. Rev. D* **68** (2003), 046005. DOI: 10.1103/PhysRevD.68.046005, arXiv: hep-th/0301240.
6. S. B. Giddings, S. Kachru and J. Polchinski, "Hierarchies from fluxes in string compactifications," *Phys. Rev. D* **66** (2002), 106006. DOI: 10.1103/PhysRevD.66.106006, arXiv: hep-th/0105097.
7. S. Kachru, R. Kallosh, A. Linde, J. Maldacena, L. McAllister and S. P. Trivedi, "Towards inflation in string theory," *JCAP* **10** (2003), 013. DOI: 10.1088/1475-7516/2003/10/013, arXiv: hep-th/0308055.
8. K. Dasgupta, J. P. Hsu, R. Kallosh, A. Linde and M. Zagermann, "D3/D7 brane inflation and semilocal strings," *JHEP* **08** (2004), 030. DOI: 10.1088/1126-6708/2004/08/030, arXiv: hep-th/0405247.
9. A. R. Frey, M. Lippert and B. Williams, "The Fall of Stringy de Sitter," *Phys. Rev. D* **68** (2003), 046008. DOI: 10.1103/PhysRevD.68.046008, arXiv: hep-th/0305018.
10. N. J. Hitchin, "The geometry and topology of moduli spaces," in *Global Geometry and Mathematical Physics*, Lecture Notes in Mathematics **1451**, Springer, Berlin (1990), 1–48. DOI: 10.1007/BFb0085064; R. Britto, B. Feng, O. Lunin and S. J. Rey, "U(N) instantons on N=1/2 superspace: Exact solution and geometry of moduli space," *Phys. Rev. D* **69** (2004), 126004. DOI: 10.1103/PhysRevD.69.126004, arXiv: hep-th/0311275; S. Parvizi, "Noncommutative instantons and the information metric," *Mod. Phys. Lett. A* **17** (2002), 341–354. DOI: 10.1142/S0217732302006436, arXiv: hep-th/0202025.
11. T. Jacobson, "Introduction to Quantum Fields in Curved Spacetime and the Hawking Effect," arXiv: gr-qc/0308048.

TTMP vol 3 (2), 2026
doi: 10.30511/TTMP.2026.2088786.1076

Transactions in Theoretical and Mathematical Physics

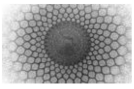

Qualitative Analysis of the Effect of Minimising Listeriosis in Cow Population on the Eradication of Human Listeriosis

Abayomi Ayotunde Ayoade[a,1]

[1]Department of Mathematics, Faculty of Physical and Earth Sciences, University of Lagos, Lagos, Nigeria

Received: 10 May 2026 / Accepted: 15 May 2026/ Published:17 May 2026

Abstract Listeriosis is a bacterial infection and one of the key zoonotic foodborne diseases, accounting for about 28% of yearly food-related mortality in the US. Listeriosis spreads into human populations mostly through the ingestion of contaminated milk and meat. Since cows are a major source of milk and meat to humans, a nonlinear epidemic model is designed to analyse the transmission dynamics of listeriosis in cow populations under management conditions of treatment and disinfection. The model is studied qualitatively by deriving its equilibria and reproductive ratio (R_0), and by analysing its stability using stability theory for differential equations. The analysis reveals the necessary and sufficient conditions for listeriosis persistence and eradication in cow populations. The results indicate that listeriosis spread in cow populations could be prevented or eradicated if the rates of application of treatment and disinfection exceed certain critical values.

Keywords: Listeriosis; model; equilibria; reproductive ratio; stability

1 Introduction

Listeriosis is a contagious infection that instigates stillbirths in mammals. The agent of listeriosis is *Listeria monocytogenes*, which survives in soil and water and attacks the intestinal track through the ingestion of contaminated food materials [1]. Listeriosis persists as a major issue in veterinary medicine and as one of the key zoonotic food-borne diseases, accounting for about 28% of food-related mortality in the US each year [2]. It is a serious foodborne disease, and studies have established a link between ingestion of contaminated silage and animal rhombencephalitis [3].

[a]ayoayoade@unilag.edu.ng

While cattle play a crucial role in spreading and amplifying the listeria bacteria, *L. monocytogenes* is a saprophyte, meaning it thrives and naturally survives as a free-living organism in soil, mud, and water [4, 5]. The bacteria are highly resilient and can persist in dry soil, manure, and on straw for long periods, continuously seeding the infection into animal feed [6, 7]. While listeriosis is a serious infection in certain individuals, humans do not typically contract it through direct contact with cattle; rather, they are infected through foodborne transmission [8, 9].

The incubation period for listeriosis is between 11–70 days, and the most vulnerable individuals are the elderly, babies, pregnant women and immunosuppressed patients such as individuals who are suffering from AIDS, hemochromatosis, cirrhosis, diabetes, sarcoidosis, renal failure, aplastic anaemia, hematologic malignancies, ulcerative colitis and collagen vascular disease [10–12]. When the infection is fully developed, infected cows may exhibit meningitis, febrile gastroenteritis, sepsis, perinatal infections, etc. [13]. *L. monocytogenes* infections in cows may be treated with antibiotics such as rifampicin, linezolid and meropenem [11].

Listeriosis outbreaks have been reported in Europe, Japan, North America, and South Africa, where 209 deaths were attributed to listeriosis infections between 2017 and 2018 [14]. Several mathematical and nonmathematical models have been developed to give insights into the transmission dynamics, growth and survival of *L. monocytogenes*. The majority of the mathematical models in the literature consider listeriosis transmission in the environment and in human and animal populations, without considering any particular animal [2, 11, 13, 14]. Since listeriosis spreads into the human population mostly through the ingestion of contaminated milk and meat [15] and given that cows are a major source of milk and meat to humans, it is reasonable to argue that elimination of *L. monocytogenes* in cow populations may be enough to prevent or eradicate listeriosis in

the human population. Based on that hypothesis, a nonlinear epidemic model is developed by incorporating factors capable of preventing or eradicating listeriosis in cow populations; in the present analysis, unlike earlier works, the dynamics of listeriosis in the environment and in human and animal populations are considered. The management conditions incorporated into the present model are vaccination of calves, treatment of cows, and disinfection of the environment.

2 Model Formulation

The population $N(t)$ that consists of cows and contaminated environment in Fig. (1) is divided into five compartments: susceptible cows (S_c), vaccinated cows (V_c), infected cows (I_c), recovered cows (R_c) and contaminated environment (C_e). Cows are recruited at rate π, with some proportion α vaccinated at birth and moved to the vaccination class V_c with the quantity $\alpha\pi$, while the remaining proportion $(1-\alpha)$ moves to the susceptible compartment at birth with the quantity $(1-\alpha)\pi$. The proportion α of the cows that are vaccinated at birth is immune to listeriosis infection until the immunity wanes. The vaccinated cows move to the susceptible compartment at a rate ρ after waning of immunity. Infections occur when there is effective contact between susceptible and infected cows, and between susceptible cows and a contaminated environment, at rates β_1 and β_2, respectively.

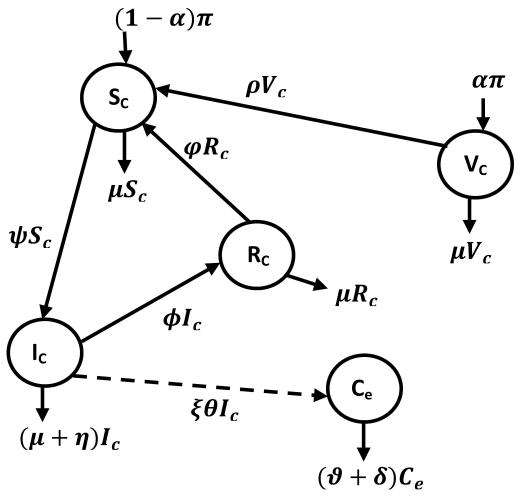

Fig. 1 Transmission diagram of listeriosis dynamics in cow populations

Infected cows increase *L. monocytogenes* in the soil at rate θ and regain susceptibility after recovery at rate φ. Treatment and disinfection are introduced to the infected cows and the environment at rates ϕ and ϑ, respectively, and the introduction of the two controls results in reductions in disease spread from the infected cows and the contaminated environment, with reduction factors τ_1 and τ_2, respectively. The reduction factors τ_1 and τ_2 are embedded in ψ. The introduction of treatment ϕ to the infected cows also reduces θ, the rate at which the infected cows increase the growth of *L. Monocytogenes* in the environment with reduction factor ξ. Mortality unrelated to listeriosis in cows occurs at rate μ while listeriosis-related mortality in cows occurs at rate η. Also, listeriosis removal from the soil unrelated to disinfection occurs at rate δ. Going by the aforementioned assumptions and the transmission diagram, the following nonlinear epidemic model is derived.

$$\frac{dV_c}{dt} = \alpha\pi - (\rho+\mu)V_c, \tag{1}$$

$$\frac{dS_c}{dt} = (1-\alpha)\pi + \rho V_c + \varphi R_c - (\psi+\mu)S_c, \tag{2}$$

$$\frac{dI_c}{dt} = \psi S_c - (\phi+\xi\theta+\eta+\mu)I_c, \tag{3}$$

$$\frac{dR_c}{dt} = \phi I_c - (\varphi+\mu)R_c, \tag{4}$$

$$\frac{dC_e}{dt} = \xi\theta I_c - (\vartheta+\delta)C_e, \tag{5}$$

where

$$\psi = \tau_1\beta_1 I_c + \tau_2\beta_2 C_e. \tag{6}$$

2.1 Positivity and Boundedness of Solutions

Theorem 1 *The listeriosis model in Eq. (1)-Eq. (5) is bounded in the region*

$$\Omega = \Big\{(V_c,S_c,I_c,R_c,C_e)\in\mathbb{R}^5 :\ 0<S_c\le\frac{\pi}{\mu},\quad 0\le V_c<1,\quad 0\le I_c<1,\quad 0\le R_c<1,\quad 0\le C_e\le\frac{\xi\theta}{\vartheta+\delta}\Big\}. \tag{7}$$

if it is established that the solutions of the model are nonnegative.

Proof Let the solution set of the model be $\{V_c(t),S_c(t),I_c(t),R_c(t),C_e(t)\}$. Since the model monitors the populations of living things, the initial conditions to each state variable are nonnegative, i.e., $V_c(0)\ge 0$, $S_c(0)\ge 0$, $I_c(0)\ge 0$, $R_c(0)\ge 0$, and $C_e(0)\ge 0$.
From Eq. (1),

$$\frac{dV_c(t)}{dt} = \alpha\pi - (\rho+\mu)V_c, \tag{8}$$

$$\frac{dV_c(t)}{dt} + \sigma V_c(t) = \varepsilon, \tag{9}$$

where $\sigma = \rho + \mu$ and $\varepsilon = \alpha\pi$. Then,

$$\Rightarrow \frac{dV_c(t)}{dt}\exp(\sigma t) + \sigma V_c(t)\exp(\sigma t) = \varepsilon \exp(\sigma t), \tag{10}$$

$$\Rightarrow \frac{d}{dt}\left[V_c(t)\exp(\sigma t)\right] = \varepsilon \exp(\sigma t), \tag{11}$$

$$\Rightarrow V_c(t) = V_c(0)\exp(-\sigma t) + \frac{\varepsilon}{\sigma}\left[1 - \exp(-\sigma t)\right]. \tag{12}$$

Therefore, $V_c(t) \geq 0$ in Eq. (12) since $V_c(0) \geq 0$. Hence, the solution $V_c(t)$ is nonnegative. By the same argument, the nonnegativity for other solutions $S_c(t)$, $I_c(t)$, $R_c(t)$, and $C_e(t)$ can be established. Hence, the solution set $\{V_c(t), S_c(t), I_c(t), R_c(t), C_e(t)\}$ for the model is nonnegative. Therefore, the model is bounded in the region defined in Eq. (7).

3 Model Analysis

3.1 Equilibria and Reproductive Ratio

The listeriosis model Eq. (1)-Eq. (5) allows a listeriosis-free equilibrium (LFE) obtained as $L_0 = \left(V_c^0, S_c^0, I_c^0, R_c^0, C_e^0\right) = \left(\frac{\alpha\pi}{\mu+\rho}, \frac{(\mu+\rho)(1-\alpha)\pi+\rho\alpha\pi}{\mu(\mu+\rho)}, 0, 0, 0\right)$ and a listeriosis-endemic equilibrium (LEE) obtained as $L^* = \left(V_c^*, S_c^*, I_c^*, R_c^*, C_e^*\right)$ with coordinates

$$V_c^* = \frac{\alpha\pi}{\mu+\rho} > 0, \tag{13}$$

$$S_c^* = \frac{(\mu+\rho)(1-\alpha)\pi + \rho\alpha\pi + \varphi(\mu+\rho)R_c^*}{(\mu+\rho)(\psi+\mu)} > 0, \tag{14}$$

$$I_c^* = \frac{\psi S_c^*}{\phi + \xi\theta + \eta + \mu} > 0, \tag{15}$$

$$R_c^* = \frac{\phi I_c^*}{\varphi + \mu} > 0, \tag{16}$$

$$C_e^* = \frac{\xi\theta I_c^*}{\vartheta + \delta} > 0. \tag{17}$$

After deriving the model's equilibria, the reproductive ratio (R_0) must be computed to quantify the tendency toward listeriosis outbreaks or eradication in cow populations. It is an epidemiological parameter that measures the transmission potential of infectious diseases. If the numerical value of R_0 is greater than one, the infection will spread, but if $R_0 < 1$, the infection will fail to spread or die out. Following the Next Generation Matrix Operator developed by Driessche and Watmough, which has been applied in many epidemic models [16–21] and outlined in [22], the reproductive ratio for the present listeriosis model is derived and is given by

$$R_0 = \frac{(\vartheta+\delta)\tau_1\beta_1 S_c^0 + \xi\theta\tau_2\beta_2 S_c^0}{(\vartheta+\delta)(\phi+\xi\theta+\eta+\mu)}. \tag{18}$$

The result of R_0 in Eq. (18) indicates that listeriosis transmission can be prevented or eradicated in cow populations if the treatment and disinfection parameters, ϕ and ϑ, are sufficiently large. Increasing these parameters reduces the effective transmission rates β_1 and β_2 associated with infected cows and the contaminated environment, respectively, as well as the parameter θ, which governs the contribution of infected cows to the growth of *L. monocytogenes* in the environment. Consequently, higher values of ϕ and ϑ lead to lower effective values of β_1, β_2, and θ, thereby decreasing the magnitude of R_0. If R_0 is reduced below unity, as indicated by Eq. (18), listeriosis transmission cannot be sustained, providing a necessary condition for the prevention or eradication of the disease in cow populations.

3.2 Stability Analysis of Listeriosis-Free Equilibrium

Theorem 2 *The listeriosis-free equilibrium of the model is locally asymptotically stable if the associated $R_0 < 1$; otherwise the model is locally asymptotically unstable.*

Proof To investigate the stability of the model about the listeriosis-free equilibrium L_0, the variational matrix of the model about L_0 is derived and is given as

$$J(L_0) = \begin{pmatrix} -(\mu+\rho) & 0 & 0 & 0 & 0 \\ \rho & -\mu & -\tau_1\beta_1 S_c^0 & \varphi & -\tau_2\beta_2 S_c^0 \\ 0 & 0 & \tau_1\beta_1 S_c^0 - \Gamma & 0 & \tau_2\beta_2 S_c^0 \\ 0 & 0 & \phi & -(\varphi+\mu) & 0 \\ 0 & 0 & \xi\theta & 0 & -(\vartheta+\delta) \end{pmatrix}, \tag{19}$$

where $\Gamma = \phi + \xi\theta + \eta + \mu$.
Three of the eigenvalues of the matrix $J(L_0)$ are negative and are given as $-\mu$, $-(\mu+\rho)$ and $-(\varphi+\mu)$. The remaining two eigenvalues can be computed from the submatrix

$$A = \begin{pmatrix} \tau_1\beta_1 S_c^0 - (\phi+\xi\theta+\eta+\mu) & \tau_2\beta_2 S_c^0 \\ \xi\theta & -(\vartheta+\delta) \end{pmatrix}. \tag{20}$$

$|A - \lambda I| = 0$ is evaluated to

$$\begin{aligned} \lambda^2 + \left[\vartheta+\delta+\phi+\xi\theta+\eta+\mu-\tau_1\beta_1 S_c^0\right]\lambda \\ + (\vartheta+\delta)(\phi+\xi\theta+\eta+\mu) \\ - (\vartheta+\delta)\tau_1\beta_1 S_c^0 - \xi\theta\tau_2\beta_2 S_c^0 = 0. \end{aligned} \tag{21}$$

All the roots in Eq. (21) are less than zero if

$$\vartheta+\delta+\phi+\xi\theta+\eta+\mu-\tau_1\beta_1 S_c^0 > 0. \tag{22}$$

and,

$$\begin{aligned} &(\vartheta+\delta)(\phi+\xi\theta+\eta+\mu) \\ &- (\vartheta+\delta)\tau_1\beta_1 S_c^0 - \xi\theta\tau_2\beta_2 S_c^0 > 0. \end{aligned} \tag{23}$$

From Eq. (23),

$$\begin{aligned}&(\vartheta+\delta)\tau_1\beta_1 S_c^0+\xi\theta\tau_2\beta_2 S_c^0\\&\qquad<(\vartheta+\delta)(\phi+\xi\theta+\eta+\mu)\\&\Rightarrow\frac{(\vartheta+\delta)\tau_1\beta_1 S_c^0+\xi\theta\tau_2\beta_2 S_c^0}{(\vartheta+\delta)(\phi+\xi\theta+\eta+\mu)}\\&\qquad<\frac{(\vartheta+\delta)(\phi+\xi\theta+\eta+\mu)}{(\vartheta+\delta)(\phi+\xi\theta+\eta+\mu)}.\end{aligned}\tag{24}$$

In view of Eq. (18), $R_0<1$.

Since it has been established that $R_0<1$, inequality (22) is satisfied and all eigenvalues of Eq. (21) are negative. Therefore, the listeriosis-free equilibrium of the model is locally asymptotically stable. The global stability of the listeriosis model can also be investigated around the disease-free equilibrium L_0 using a Lyapunov function.

Theorem 3 *The listeriosis-free equilibrium L_0 is globally asymptotically stable if $R_0<1$.*

Proof The model is globally asymptotically stable around L_0 if it can be shown that $\dot{V}(t)<0$, where $V(t)$ is a Lyapunov function. Define

$$\dot{V}(t)=A_1I_c'+A_2C_e',\tag{25}$$

$$\dot{V}(t)=-\Big[A_1(\phi+\xi\theta+\eta+\mu)-A_1\tau_1\beta_1S_c^0-A_2\xi\theta\Big]I_c-\Big[A_2(\vartheta+\delta)-A_1\tau_2\beta_2S_c^0\Big]C_e,\tag{26}$$

$$\dot{V}(t)=(\vartheta+\delta)\tau_1\beta_1S_c^0C_e+\xi\theta\tau_2\beta_2S_c^0C_e-(\vartheta+\delta)(\phi+\xi\theta+\eta+\mu)C_e,\tag{27}$$

$$\dot{V}(t)=(\vartheta+\delta)(\phi+\xi\theta+\eta+\mu)\times\left[\frac{(\vartheta+\delta)\tau_1\beta_1S_c^0+\xi\theta\tau_2\beta_2S_c^0}{(\vartheta+\delta)(\phi+\xi\theta+\eta+\mu)}-1\right]C_e,\tag{28}$$

$$\dot{V}(t)=(\vartheta+\delta)(\phi+\xi\theta+\eta+\mu)(R_0-1)C_e.\tag{29}$$

In view of Eq. (18),

$$\dot{V}(t)=(\vartheta+\delta)(\phi+\xi\theta+\eta+\mu)(R_0-1)C_e.\tag{30}$$

If $R_0\leq1$ in Eq. (30), the Lyapunov function satisfies $\dot{V}(t)\leq0$. Also, $\dot{V}(t)=0$ if $C_e=0$. Therefore, the listeriosis-free equilibrium of the model is globally asymptotically stable. However, if $R_0\geq1$, there exists a unique listeriosis-endemic equilibrium.

3.3 Stability Analysis of Listeriosis-Endemic Equilibrium

Theorem 4 *The listeriosis-free equilibrium becomes unstable and the system moves from L_0 to L^*, the listeriosis-endemic equilibrium, if $R_0>1$.*

Proof The reproductive ratio is greater than one ($R_0>1$) and the listeriosis-endemic equilibrium of the model is locally asymptotically stable if it is established that all the The eigenvalues of the variational matrix of the model about L^*, the listeriosis-endemic equilibrium, are negative. The variational matrix of the model computed at L^* is derived as

$$J(L^*)=\begin{pmatrix}-\mu-\rho&0&0&0&0\\\rho&-\psi-\mu&-\tau_1\beta_1S_c^*&\varphi&-\tau_2\beta_2S_c^*\\0&\psi&\tau_1\beta_1S_c^*-\Gamma&0&\tau_2\beta_2S_c^*\\0&0&\phi&-\varphi-\mu&0\\0&0&\xi\theta&0&-\vartheta-\delta\end{pmatrix}.\tag{31}$$

One of the eigenvalues of $J(L^*)$ is $-(\mu+\rho)$ and the remaining eigenvalues can be derived from submatrix M defined as

$$J(M)=\begin{pmatrix}-(\psi+\mu)&-\tau_1\beta_1S_c^*&\varphi&-\tau_2\beta_2S_c^*\\\psi&\tau_1\beta_1S_c^*-\Gamma&0&\tau_2\beta_2S_c^*\\0&\phi&-(\varphi+\mu)&0\\0&\xi\theta&0&-(\vartheta+\delta)\end{pmatrix}.\tag{32}$$

Since a row reduction transform a matrix into a new one that has the exact same solution set with the original matrix, we row reduce $J(M)$ in (32) and obtain

$$J(M)=\begin{pmatrix}-(\psi+\mu)&-\tau_1\beta_1S_c^*&\varphi&-\tau_2\beta_2S_c^*\\0&c_1&\varphi&c_2\\0&\phi&-(\varphi+\mu)&0\\0&\xi\theta&0&-(\vartheta+\delta)\end{pmatrix},\tag{33}$$

where

$$c_1=\frac{(\psi+\mu)\big[\tau_1\beta_1S_c^*-(\phi+\xi\theta+\eta+\mu)\big]}{\psi}-\tau_1\beta_1S_c^*,\tag{34}$$

$$c_2=\frac{(\psi+\mu)\tau_2\beta_2S_c^*}{\psi}-\tau_2\beta_2S_c^*.\tag{35}$$

The matrix $J(M)$ has the eigenvalue $-(\psi+\mu)$ while the remaining eigenvalues can be obtained from submatrix N defined as

$$J(N)=\begin{pmatrix}c_1&\varphi&c_2\\\phi&-(\varphi+\mu)&0\\\xi\theta&0&-(\vartheta+\delta)\end{pmatrix}.\tag{36}$$

Row reduce matrix operation reduces the matrix $J(N)$ to

$$J(N)=\begin{pmatrix}-\frac{c_1}{\varphi}(\varphi+\mu)+\phi&0&-\frac{c_2}{\varphi}(\varphi+\mu)\\\phi&-(\varphi+\mu)&0\\\xi\theta&0&-(\vartheta+\delta)\end{pmatrix}.\tag{37}$$

The matrix $J(N)$ has one of the eigenvalues being $-(\varphi+\mu)$ and the remaining two eigenvalues can be derived from matrix P given as

$$J(P)=\begin{pmatrix}-\frac{c_1}{\varphi}(\varphi+\mu)+\phi & -\frac{c_2}{\varphi}(\varphi+\mu)\\ \xi\theta & -(\vartheta+\delta)\end{pmatrix}. \tag{38}$$

The characteristic equation of Eq. (38), i.e., $|A-\lambda I|=0$, simplifies to

$$\begin{aligned}\lambda^2+&\left[\frac{c_1}{\varphi}(\varphi+\mu)+\vartheta+\delta-\phi\right]\lambda\\ &+\frac{\xi\theta c_2}{\varphi}(\varphi+\mu)+(\vartheta+\delta)\left[\frac{c_1}{\varphi}(\varphi+\mu)-\phi\right]=0.\end{aligned} \tag{39}$$

The two eigenvalues in Eq. (39) are negative if

$$\begin{aligned}&\frac{c_1}{\varphi}(\varphi+\mu)+\vartheta+\delta-\phi>0, \text{and}\\ &\frac{\xi\theta c_2}{\varphi}(\varphi+\mu)+(\vartheta+\delta)\left[\frac{c_1}{\varphi}(\varphi+\mu)-\phi\right]>0.\end{aligned} \tag{40}$$

If inequalities (40) are true, the two eigenvalues in Eq. (39) are negative, $R_0>1$, and the endemic equilibrium of the listeriosis model is locally asymptotically stable. However, if one or both eigenvalues in Eq. (39) are positive, $R_0<1$, and the endemic equilibrium of the model is locally asymptotically unstable if one or both inequalities (40) are not true.
From inequalities (40), assuming

$$\frac{c_1}{\varphi}(\varphi+\mu)+\vartheta+\delta-\phi<0. \tag{41}$$

Then,

$$\phi^*-\vartheta^*>\frac{c_1}{\varphi}(\varphi+\mu)+\delta. \tag{42}$$

Notice in the transmission diagram (Figure 1) as well as in Eq. (4) and Eq. (5) that ϕ results in the transfer of infected cows to the recovered compartment, while ϑ results in the elimination of *L. monocytogenes* from the environment. Parameter ϕ acts as an injection (positive contribution), whereas ϑ acts as a withdrawal (negative contribution). Therefore, the quantity $\phi^*-\vartheta^*$ appearing in inequality (42) does not represent a net difference between the two controls, but rather the critical threshold condition that must be satisfied for R_0 to be reduced below unity and for the endemic equilibrium to lose its local asymptotic stability. While ϕ^* denotes the critical treatment level required to transfer infected cows into the recovered compartment, ϑ^* denotes the critical disinfection level required to eliminate *L. monocytogenes* from the environment. Consequently, the stability of the endemic equilibrium depends on the magnitude of the treatment and disinfection parameters ϕ and ϑ. If the threshold condition (42) is satisfied, one or both eigenvalues in Eq. (39) become positive and the endemic equilibrium is locally asymptotically unstable. Conversely, if condition (42) is not satisfied, the eigenvalues in Eq. (39) may remain negative and the endemic equilibrium may be negative and the endemic equilibrium of the listeriosis model becomes locally asymptotically stable.

4 Results and Discussion

Based on the hypothesis underlying the model, eradication of *L. monocytogenes* in cow populations may be enough to prevent or eradicate listeriosis in the human population. A rigorous analysis was conducted, and the necessary conditions for local and global stability of the model were derived, which depended on the threshold parameter R_0. The disease-free equilibrium of the model was proved to be locally and globally asymptotically stable whenever $R_0<1$. The implication of the disease-free equilibrium being locally and globally asymptotically stable is that listeriosis would fail to spread within the model framework in both local and global cattle farms if a listeriosis-infected cow were introduced into a naive cow population. Listeriosis would not break out locally and globally in cow populations if the conditions imposed on the model were maintained. The stability of the disease-free equilibrium therefore depended on the rates of applications of treatment and disinfection parameters whose values must attain the critical level defined in the analysis (i.e., ϕ^* and ϑ^*). If the values of the control parameters treatment and disinfection fall short of these critical levels, the disease-free equilibrium would become unstable. *L. monocytogenes* might spread in cow populations and consequently get into the human population when the disease-free equilibrium becomes unstable.

5 Conclusion

Listeriosis is a widespread zoonotic disease. The main natural reservoirs are soil, water, decaying vegetation and the gastrointestinal tracts of animals. A wide range of animals – both domestic and wild – act as reservoirs and asymptomatic carriers, shedding the bacteria into the environment via faeces, milk, and uterine discharges [1, 3]. Examples of animals (both domestic and wild as well as farm animals) that are carriers for *L. monocytogenes* are sheep, cattle, goats, pigs, dogs, cats, poultry, deer, moose, elk, reindeer, wild boars, mice, rabbits, rats, gulls, crows, pigeons, fish, crustaceans, insects, etc. [3, 10]. While animals rarely transmit listeriosis directly to humans, humans typically contract listeriosis by consuming food or water contaminated by these animal reservoirs. Because cattle are a major reservoir that transmits the bacteria into raw milk, unpasteurised dairy products, and

meat, a compartmental model has been designed to analyse the transmission dynamics of listeriosis in cow populations under management conditions of treatment and disinfection. The solutions of the model had been proved to be positive and bounded. The equilibria and reproductive ratio of the model were derived, and the stability was analysed based on the derived reproductive ratio. The model's stability had been analysed to theoretically derive the minimum level of treatment and disinfection needed to eradicate human listeriosis by preventing or minimising listeriosis in the cow population. The model analysis had been limited to qualitative aspects, while the quantitative and numerical simulations had been excluded to reduce space, as in [20, 23–25]. However, it is anticipated that this analysis has provided the essential knowledge required to prevent listeriosis transmission in the human population by preventing or minimising listeriosis spread in the cow population.

References

1. H. Hof (2001). Listeria monocytogenes: a causative agent of gastroenteritis? *European Journal of Clinical Microbiology and Infectious Diseases*, 20(6), 369–373. DOI: 10.1007/PL00011277.
2. S. Osman, O.D. Makinde & D.M. Theuri (2018). Stability analysis and modelling of listeriosis dynamics in human and animal populations. *Global Journal of Pure and Applied Mathematics*, 14(1), 115–138.
3. M.L. Rossi, A. Paiva, M. Tornese, S. Chianelli & A. Troncoso (2008). Listeria monocytogenes outbreak: a review of the routes that favour bacterial presence. *Revista Chilena de Infectologia*, 25(2), 328–335. DOI: 10.4067/S0716-10182008000500002.
4. J.K.K. Asamoah, E. Addai, Y.D. Arthur & E. Okyere (2023). A fractional mathematical model for listeriosis infection using two kernels. *Decision Analytics Journal*, 6, 100191. DOI: 10.1016/j.dajour.2023.100191.
5. P.J. Witbooi, C. Africa, A. Christoffels & I.H.I. Ahmed (2020). A population model for the 2017/18 listeriosis outbreak in South Africa. *PLoS ONE*, 15(3), e0229901. DOI: 10.1371/journal.pone.0229901.
6. Z. Meng, S. Lyu, M. Zhang, X. Li & Q. Zhang (2024). Sufficient and necessary conditions of near-optimal controls for a stochastic listeriosis model with spatial diffusion. *Electronic Research Archive*, 32(5), 3059–3091. DOI: 10.3934/era.2024140.
7. C.W. Chukwu, J. Mushanyu, M.L. Juga & Fatmawati (2020). A mathematical model for co-dynamics of listeriosis and bacterial meningitis diseases. *Communications in Mathematical Biology and Neuroscience*, 2020, 83. DOI: 10.28919/cmbn/5060.
8. S.Y. Tchoumia, C.W. Chukwu & Windarto (2024). A multi-population approach to epidemiological modeling of listeriosis transmission dynamics incorporating food and environmental contamination. *Healthcare Analytics*, 5, 100344. DOI: 10.1016/j.health.2024.100344.
9. K.N. Sachin, M. Mulimani, S. Kumbinarasaiah, D.K. Suguntha & N. Lavanya (2026). Homotopy analysis method on listeria infection model caused by pre-cooked package food. *Journal of Nonlinear Modeling and Analysis*, 8(2), 520–550. DOI: 10.12150/jnma.2026.520.
10. J. Pichler, A. Pietka & F. Allerberger (2011). Lesson to be learned from an outbreak of foodborne listeriosis, Austria 2009–2010. *Food Protection Trends*, 31(5), 268–273.
11. B.E. Bassey (2020). Dynamic optimal control for multi-chemotherapy treatment of dual listeriosis infection in human and animal population. *Applications and Applied Mathematics*, 15(1), 192–225.
12. S. Osman & O.D. Makinde (2018). A mathematical model for coinfection of listeriosis and anthrax diseases. *International Journal of Mathematics and Mathematical Sciences*, 2018, 1–14. DOI: 10.1155/2018/1725671.
13. O. Osman & C. Sebil (2020). Analysis of listeriosis transmission dynamics with optimal control. *Applied Mathematics*, 11, 712–737. https://doi.org/10.4236/am.2020.117048
14. C.W. Chukwu & F. Nyabadza (2020). A theoretical model of listeriosis driven by cross contamination of ready-to-eat food products. *International Journal of Mathematics and Mathematical Sciences*, 2020, 1–14. DOI: 10.1155/2020/8869751.
15. B. Swaminathan & P. Gerner-Smidt (2007). The epidemiology of human listeriosis. *Microbes and Infection*, 9(10), 1236–1243. DOI: 10.1016/j.micinf.2007.05.011.
16. A.A. Ayoade, S.O. Agboola & T. Srinivasarao (2025). Bifurcation for a disease model with the effect of mass media. *Math. & Comput. Sci.*, 6(3), 89–103. DOI: 10.30511/mcs.2025.2055529.1318.
17. O.M. Ogumiloro & A.A. Ayoade (2025). Qualitative and numerical observations into the career trajectories of early career academics: A mathematical model approach. *Tanzania Journal of Science*, 51(3), 1101–1112. DOI: 10.65085/2507-7961.1131.
18. A.A. Ayoade, T. Srinivasarao & Z. Shah (2025). Modeling the influence of treatment accessibility and treatment compliance on the dynamics of HIV/AIDS. *Journal of Nonlinear Modeling and Analysis*, 7(2), 552–582. DOI: 10.12150/jnma.2025.552.
19. A.A. Ayoade & M.O. Ibrahim (2023). Modeling the dynamics and control of rabies in dog population within and around Lagos, Nigeria. *Eur. Phys. J. Plus*, 138, 397. DOI: 10.1140/epjp/s13360-023-03956-8.
20. A.A. Ayoade & M.O. Ibrahim (2022). Analysis of transmission dynamics and mitigation success of COVID-19

in Nigeria: An insight from a mathematical model. *The Aligarh Bulletin of Mathematics*, 41(1), 81–106.

21. K. Gurski & K. Homan (2023). Staged HIV transmission and treatment in a dynamic model with long-term partnerships. *Journal of Mathematical Biology*, 86, 74. DOI: 10.1007/s00285-023-01885-w.
22. A.A. Ayoade, S.O. Agboola & M.O. Ibrahim (2019). Mathematical analysis of the effect of maternal immunity on the global eradication of measles. *Annals. Computer Science Series*, 17th Tome, 1st Fasc.
23. A.A. Ayoade (2022). Integer and fractional order models for rabies: a theoretical approach. *Mathematics and Computational Sciences*, 2(1), 1–9. DOI: 10.30511/mcs.2021.541111.1046.
24. A.A. Ayoade, M.O. Ibrahim & O. Odetunde (2018). Analytical solution of a fractional order cholera model. *Nigerian Journal of Scientific Research*, 17(2), 158–164.
25. A.A. Ayoade, S.A. Agunbiade & T. Oyedepo. Backward bifurcation in epidemic models of *Toxoplasma gondii*: a qualitative analysis. *Journal of Nepal Mathematical Society*, 5(1), 1–9. DOI: 10.3126/jnms.v5i1.47369.
26. T. Srinivasarao (2020). On an ecological model of mutualism between two species with a mortal predator. *Applications and Applied Mathematics*, 15(2), 1309–1322.

TTMP vol 3 (2), 2026
doi: 10.30511/TTMP.2026.2088274.1075

Transactions in Theoretical and Mathematical Physics

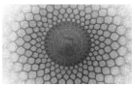

A Discussion on the Eigenvalues of Sum Operators in the Hilbert space

Hanie Jarollahi,[1], **Mehdi Jafari Matehkolaee**[a2]

[1]Department of Physics, Iran University of Science and Technology, Tehran, 16846-13214, Narmak, Iran
[2]Department of Physics and Energy Engineering, Amirkabir University of Technology (Tehran Polytechnic) Hafez Avenue, Tehran, Iran

Received: 08 May 2026 / Accepted: 15 May 2026 / Published: 19 May 2026

Abstract In this paper, we present rigorous proofs and counterexamples showing that the notion of partiality (reductionism) does not apply to operators in Hilbert space. We argue that the classical concepts of partiality and totality (holism) are fundamentally incompatible with the structure of quantum mechanics. This claim is supported across different interpretations of quantum theory, including cases involving nonlinear operators. Our analysis highlights the limitations of classical intuition in operator algebra and provides a refined understanding of eigenvalue behavior in quantum systems.

Keywords: Eigenvalues; Holism; Reductionism

1 Introduction

Whenever a system S is composed of components S_1 and S_2, it is often written as $S = S_1 + S_2$.

In this context, operator algebra displays properties that differ sharply from classical intuition. This is particularly evident in the behavior of inverse operators [1, 2] and nonlinear operators [3, 4]. For two arbitrary operators A and B in Hilbert space, their sum is

$$C = A + B. \tag{1}$$

A careful analysis of operator algebra reveals that even linear operators in Hilbert spaces display subtleties rarely emphasized in standard quantum mechanics textbooks. For example, the adjoint of the sum of two linear operators need not equal the sum of their adjoints. In fact, while for bounded operators one routinely has

$$(A+B)^\dagger = A^\dagger + B^\dagger,$$

the statement need not hold for densely defined (unbounded) operators without further hypothesis. This departure from classical additivity has important implications; for example, this point is treated carefully in classical perturbation theory [5] and functional analysis [6].

The spectral behavior of operator sums highlights an even deeper issue. Weyl's inequalities [7] and the min–max principle [8] provide useful upper and lower bounds on the eigenvalues of sums of Hermitian operators, but these results do not imply any simple additive law. Even if both are positive, counterexamples show that they may still admit negative eigenvalues [2, 9]. This observation undermines the reductionist expectation that the extremal eigenvalues of a composite operator must reflect those of its parts.

Furthermore, modern research has shown that estimating extremal eigenvalues remains nontrivial even in structured cases. For example, new lower bounds for the minimum singular value and minimum eigenvalue have recently been obtained in matrix analysis [3, 4, 10, 11]. Algorithmic approaches now provide sharper monotone bounds for the minimum eigenvalue of M-matrices [10], while investigations of non-Hermitian perturbations demonstrate that small changes to one operator can produce dramatic spectral shifts in their sum [11]. These studies reinforce the fact that spectral properties of operator sums cannot be reduced to a straightforward "part–whole" relation, but instead demand careful operator-theoretic analysis.

In particular, this paper investigates the behavior of the smallest eigenvalue of the sum of two operators. Counterexamples show that the minimum eigenvalue of $A + B$ (or AB) does not necessarily correspond to the eigenvalues of A or B individually. Despite the importance of this issue, such operator-theoretic details have not received the attention they deserve in standard quantum mechanics presentations. By clarifying these subtleties, our work emphasizes

[a]m.matehkolaee@aut.ac.ir

the limitations of classical reductionism and highlights the emergent character of quantum operator spectra.

2 Main Issues

Suppose the smallest eigenvalue of operator A is denoted by a, and the smallest eigenvalue of operator B is b. In this case, what is the smallest eigenvalue of the operator $C = A + B$?

At first, it seems that the answer to the above question is $c = a + b$, but we will see that we obtain a controversial result.

So, we start the discussion with the example of matrices A and B:

$$A = \begin{pmatrix} 1 & 0 \\ 0 & 0 \end{pmatrix}, \qquad B = \begin{pmatrix} 4x & -x \\ 6x & -x \end{pmatrix}. \tag{2}$$

The eigenvalues of matrix A are denoted by $\lambda_a = 0, 1$, and the eigenvalues of matrix B are denoted by $\lambda_b = x, 2x$. For all $x > 0$, these eigenvalues are non-negative. We now construct the matrix $A + B$.

$$A + B = \begin{pmatrix} 1+4x & -x \\ 6x & -x \end{pmatrix}. \tag{3}$$

The eigenvalue equation of matrix (3) is given by

$$\lambda_c^2 - \lambda_c(3x+1) + 2x^2 - x = 0. \tag{4}$$

For sufficiently small x, the eigenvalues can be expanded as

$$\begin{cases} \lambda_{c,1} = \dfrac{8x + 2 + o(x)}{2} = 1 + 4x + o(x), \\ \lambda_{c,2} = \dfrac{-2x + \dfrac{x^2}{2} + o(x)}{2} = -x + o(x). \end{cases} \tag{5}$$

where $o(x)$ denotes a function that converges to zero more rapidly than x.

Thus, for small positive values of x, one of the eigenvalues of $A + B$ becomes negative, even though all eigenvalues of A and B were non-negative. This demonstrates that the smallest eigenvalue of $A + B$ cannot, in general, be expressed as the sum of the smallest eigenvalues of A and B.

A special situation: Now assume that both A and B are Hermitian operators. We define the functions f and g in terms of vectors $|u\rangle$ in the Hilbert space as follows:

$$f(u) = \frac{\langle u|Au\rangle}{\langle u|u\rangle}, \qquad g(u) = \frac{\langle u|Bu\rangle}{\langle u|u\rangle}. \tag{6}$$

Because A is Hermitian, it admits an orthonormal basis of eigenvectors $\{|u_i\rangle\}$ with eigenvalues a_i.

Any vector $|u\rangle$ can be expanded as

$$A|u_i\rangle = a_i|u_i\rangle, \qquad u = \sum_i C_i|u_i\rangle. \tag{7}$$

Substituting (7) into (6), we obtain

$$f(u) = \frac{\sum_{i,j} C_i C_j^* \langle u_j|u_i\rangle}{\sum_{i,j} C_i C_j \langle u_j|u_i\rangle} = \frac{\sum_i a_i |C_i|^2}{\sum_i |C_i|^2}. \tag{8}$$

This immediately shows that $a \leq f(u) \leq a'$, by the same reasoning $b \leq g(u) \leq b'$, where b and b' are, respectively, the smallest and largest eigenvalues of the operator B.

Now consider the operator C,

$$CV = cV. \tag{9}$$

Where V is a vector in Hilbert space similar to U. We can express this as

$$c = \frac{\langle V|CV\rangle}{\langle V|V\rangle} = f(V) + g(V). \tag{10}$$

We can directly infer from equation (10) that $a + b \leq c \leq a' + b'$.

The lower section features compelling graphs that clearly illustrate the eigenvalues of matrices A and B and $A + B$.

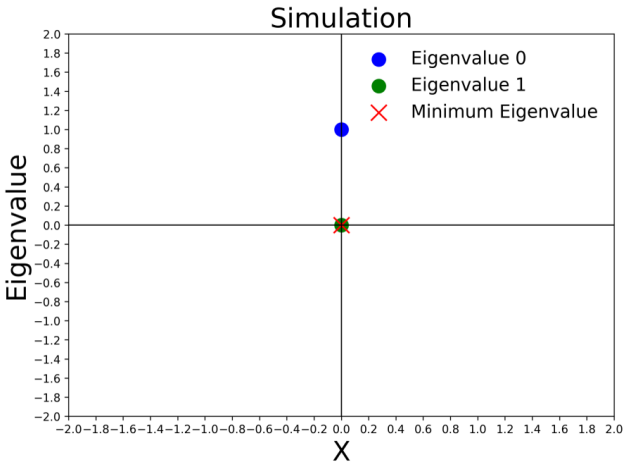

Fig. 1 This figure shows that the eigenvalues of matrix A. Direct computation yields two eigenvalues, 0 and 1, which appear as two distinct points on the axis. The smaller eigenvalue 0 is evident, contrasting with the larger eigenvalue 1.

From the x-dependence it follows that the spectrum of $A + B$ has no global minimum. For every eigenvalue identified, a smaller one appears as x increases. This graphical analysis reinforces the earlier conclusion that the smallest eigenvalue of a sum of operators cannot be simply inferred from the eigenvalues of its summands.

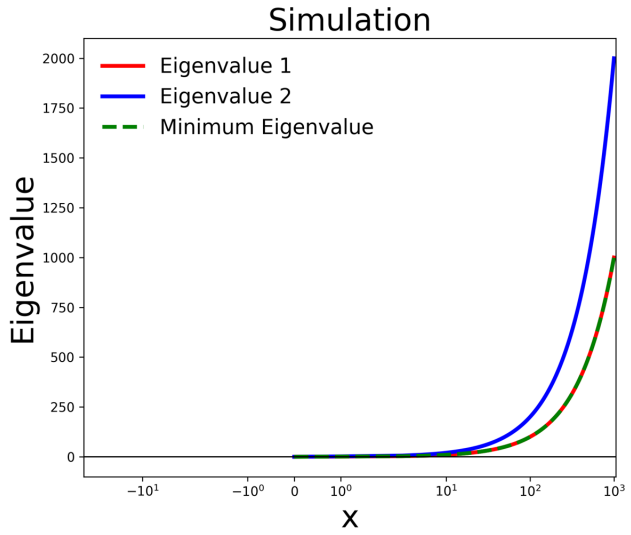

Fig. 2 This figure present the eigenvalues of matrix B. These are given by $x, 2x$. On the graph they appear as two straight lines with different slopes. Since these eigenvalues grow unbounded as $x \to \infty$, a logarithmic scale is used to display them clearly. The smaller eigenvalue x is marked with a dashed red line for emphasis.

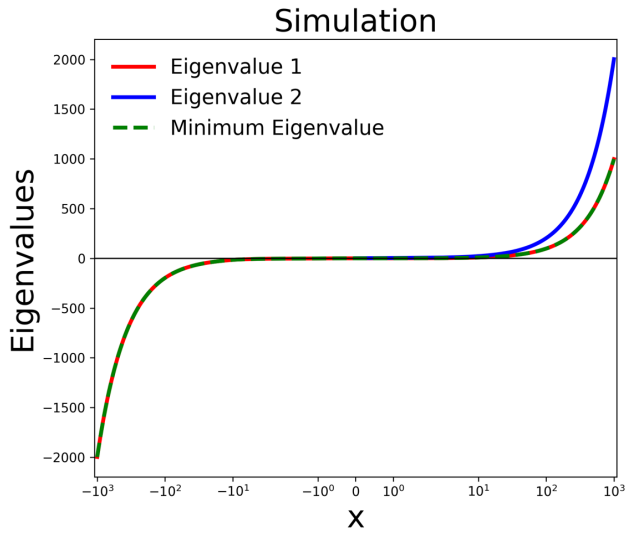

Fig. 3 This figure displays the eigenvalues of the sum $A+B$. The two eigenvalues are $1+4x$ and $-x$. The first increases linearly with x, while the second decreases without bound as $x \to \infty$. Again, a logarithmic scale is used The negative branch, $-x$, indicates that $A+B$ does not necessarily admit a non-negative minimum eigenvalue, even when both A and B possess non-negative eigenvalues.

3 Conclusion

In this paper we have shown, through explicit examples and theoretical analysis, that the spectral behavior of operator sums in Hilbert space differs fundamentally from classical expectations. In particular, the smallest eigenvalue of $A+B$ cannot, in general, be obtained as the sum of the smallest eigenvalues of A and B. Counterexamples demonstrate that even when both A and B are positive, their sum may admit negative eigenvalues. This result underscores a key distinction between classical additive structures and operator algebra in quantum mechanics.

While classical mechanics often permits decomposition of a system into independent parts, such a "part–whole" relation does not carry over straightforwardly to the spectral properties of quantum operators. Recognizing this limitation provides a clearer understanding of the mathematical foundations of quantum theory and emphasizes the need for careful operator-theoretic analysis beyond classical intuition.

References

1. J. Weidmann, *Linear Operators in Hilbert Spaces*, Springer-Verlag, New York, 1980.
2. M. H. Mortad, *Counterexamples in Operator Theory*, Birkhäuser/Springer, Cham, 2022. DOI: 10.1007/978-3-030-95750-9.
3. A. Kaur and S. H. Lui, A closer look at some new lower bounds on the minimum singular value of a matrix, *Linear Algebra and its Applications*, 2024.
4. A. Kaur and S. H. Lui, New lower bounds on the minimum singular value of a matrix, *Linear Algebra and its Applications*, 666 (2023), 62–95. DOI: 10.1016/j.laa.2023.01.017.
5. T. Kato, *Perturbation Theory for Linear Operators*, Springer, Berlin, 1995. DOI: 10.1007/978-3-642-66282-9.
6. M. Reed and B. Simon, *Methods of Modern Mathematical Physics, Vol. I: Functional Analysis*, Academic Press, New York, 1980.
7. H. Weyl, Inequalities between the two kinds of eigenvalues of a linear transformation, *Proceedings of the National Academy of Sciences of the United States of America*, 35 (1949), 408–411. DOI: 10.1073/pnas.35.7.408.
8. G. Teschl, *Mathematical Methods in Quantum Mechanics: With Applications to Schrödinger Operators*, 2nd ed., American Mathematical Society, Providence, 2014. DOI: 10.1090/gsm/157.
9. R. Bhatia, *Matrix Analysis*, Springer, New York, 1997. DOI: 10.1007/978-1-4612-0653-8.
10. Q. Zhong, An innovative algorithm for estimating the minimum eigenvalue of a general M-matrix, *Journal of Inequalities and Applications*, 2025, Article 335.
11. A. Rathore and N. Sinha, Eigenvalue behavior under non-Hermitian perturbations, *Linear Algebra and its Applications*, 670 (2024), 45–72.

TTMP vol 3 (2), 2026
doi: 10.30511/TTMP.2026.2089540.1077

Transactions in Theoretical and Mathematical Physics

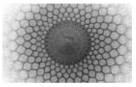

Observing an Open FRW de Sitter Universe Living in a Minkowski Spacetime

Farhang Loran[1 a]

[1] Department of Physics, Isfahan University of Technology, Isfahan 84156-83111, Iran

Received: 20 May 2026 / Accepted: 25 May 2026 / Published: 27 May 2026

Abstract We show that people living in a four dimensional Minkowski spacetime and located in the Fubini vacua of an unstable critical scalar theory, observe an open FRW de Sitter universe.

Keywords: critical scalar theory; Fubini vacua; de Sitter universe

1 Introduction

The WMAP results [1] combined with earlier cosmological observations shows that we are living in an accelerating universe. The currently observed lumpiness in the temperature of the cosmic microwave background is just right for a flat universe though there are also some evidences that our universe is spatially open [2]. The great simplifying fact of cosmology is that the universe appears to be homogeneous and isotropic along a preferred set of spatial hypersurfaces [3]. Of course homogeneity and isotropy are only approximate, but they become increasingly good approximations on larger length scales, allowing us to describe spacetime on cosmological scales by the Robertson-Walker metric. Constructing four dimensional de Sitter vacuum as a string theory (M-theory) solution has been a long standing challenge. An outstanding example of string theory models of de Sitter vacua are the KKLT models [4] with an exponentially large number of stable and metastable vacua without supersymmetry or with $\mathcal{N}=1$ supersymmetry in four dimensions, the "landscape" [5]. In KKLT models, metastable de Sitter vacua of type IIB string theory is constructed by adding $\overline{\text{D3}}$-branes to the GKP [6] model of highly warped IIB compactifications with nontrivial NS and RR three-form fluxes after certain fine tuning of the fluxes.

[a]loran@iut.ac.ir

Recently, we realized that it is possible to observe a de Sitter universe while living in a flat background. This proposal was the consequence of a simple observation: the fluctuations of the scalar field around the classical trajectory of an unstable massless ϕ^4 model in four dimensional flat Euclidean spacetime is governed by a conformally coupled scalar field theory in four dimensional de Sitter background [7]. This classical trajectory is the Fubini vacua of the classically conformal-invariant scalar field theories. In [8] S. Fubini verified that critical scalar theories possess a classical vacua with $O(D,1)$ symmetry in which the expectation value of the scalar field is non-vanishing. The motivation to study such a classical vacua at that time was "to introduce a fundamental scale of hadron phenomena by means of dilatation non-invariant vacuum state in the frame work of a scale invariant Lagrangian field theory" [8]. This result is interesting due to its uniqueness. In four dimensions, in principle, one can consider two classes of critical (classically scale-free) scalar field theories i.e. massless ϕ^4 models on Euclidean spacetime with g, the coupling constant, either positive or negative (we assume the potential $V(\phi)=-\frac{g}{4}\phi^4$). Although scalar theory with $g>0$ seems to be not physical as the potential is not bounded from below but in this case, the Euler-Lagrange equation of motion has an interesting classical solution say ϕ_0 with finite action $S[\phi_0]\sim g^{-1}$. For $g<0$, one can still consider a solution like ϕ_0 obtained by an analytic continuation from $g>0$ to $g<0$ region. But such a solution is singular on the surface of a sphere which radius is proportional to g. Consequently the action $S[\phi_0]$ is infinite and ϕ_0 can not be considered as a classical trajectory. For $g>0$ it is shown in [7] that the information geometry of the moduli space of ϕ_0 given by Hitchin formula [9] is Euclidean AdS_5,

$$\mathcal{G}_{IJ}d\theta^I d\theta^J=\frac{1}{\beta^2}\left(d\beta^2+da^2\right), \tag{1}$$

where $\theta^I \in \{\beta, a^\mu\}$ and $I = 1, \cdots, 5$. The moduli here are a_μ's the location of the center of ϕ_0 and β which is proportional to the inverse of the size of ϕ_0. This resembles the information geometry of SU(2) instantons. In addition $V(\phi_0)$ can be shown to be proportional to the SU(2) one-instanton density [10]. Interestingly, ϕ_0 is the bulk to boundary propagator in the AdS_5 geometry of the moduli space.

In ref. [11] we generalized the model to scalar theory coupled to U(1) gauge field. Such a generalization is essential as it shows how by optical observations people living in a flat Euclidean space observe a de Sitter geometry for their universe. In this model the massless scalar field is charged though we have not observed light charged scalars. This problem can be resolved noting that as we will show, in this model observations are made in a de Sitter background in which the scalar field appears to be conformally coupled to the de Sitter background. Therefore its mass is proportional to the scalar curvature R of the observed universe. Using the WKB approximation, the lifetime of the observed de Sitter background is calculated in [11] and is shown to be proportional to $e^{g^{-1}}$. (To my knowledge, this result is given for the first time in a beautiful paper by Coleman where ϕ_0 is called a "bounce" [12].) Consequently in the weak coupling limit $g \to {}^+0$ the lifetime increases exponentially.

In this paper we study the critical scalar theory on Minkowski spacetime. Here ϕ_0 is singular on a hyperbola in the timelike region which asymptotes to the lightcone. The total energy of ϕ_0, measured by an observer located at the center of ϕ_0 is conserved and vanishing though the energy density is a function of space and time. The energy density diverges in the neighborhood of singularity causing a gravitational collapse when the scalar theory is coupled to gravity. Fortunately the singularity is safe. On the one hand in Minkowski spacetime, the distance between the observers and the singularity is proportional to β. On the other hand there is some mechanism of β transition in the model: larger ϕ_0's decay to smaller ones due to say thermal fluctuations around ϕ_0 and finally there remains only a gas of zero sized bubbles which corresponds to $\beta \to \infty$. The mechanism of such transition is not clear yet but its phenomenology, probably is similar to that of the discretuum of possible de Sitter vacua in KKLT models [13]. Therefore, for the most stable ϕ_0 solution, the singularity is located at infinite future and is out of reach. Furthermore, from the observers point of view, the observable universe is an open de Sitter space which horizon is located on the singularity. Therefore they do not see the singularity at all for any value of β! Of course they should feel some back reactions when the scalar theory is coupled to gravity caused by the β transition. The energy density ρ and pressure p that they measure are constants satisfying the dark energy equation of state $\rho = -p = \Lambda$ ($8\pi G = 1$), where Λ is the cosmological constant. A question here is the value of Λ or equivalently R, the curvature scalar. At classical level, R is not determined in the critical scalar model as is expected. Because the theory is classically scale free. The quantum theory is not scale free due to loop corrections. Therefore quantum corrections are the hopeful candidates to give the value of the observed scalar curvature. The details are not clear for us yet and we postpone it to future works.

In Minkowski spacetime in the case of critical scalar model with negative coupling constant the singularity of ϕ_0 is a hyperbola in the spacelike region which asymptotes to the lightcone. One can easily verify that in this case the total energy for existence of ϕ_0 is infinite. Thus, similar to the Euclidean case, one can conclude that ϕ_0 uniquely exists only in the unstable ($g > 0$) critical scalar model.

The organization of the paper is as follows. In the next section we study the critical scalar theory on flat Euclidean background and determine the role of the moduli β in the stability of the solutions. We show that by recasting the scalar theory in terms of new fields $\tilde{\phi} = \phi - \phi_0$ at the end of the day one obtains a ϕ^4 model conformally coupled to a de Sitter background. In section 3 we switch to the Minkowski spacetime by a Wick rotation $t \to it$ and study the observed de Sitter universe in terms of the Robertson-Walker metric.

2 Critical scalar theory in $D = 4$ Euclidean space

In this section we study scalar field theories in four dimensional Euclidean space invariant under rescaling transformation $x \to x' = \lambda x$, $\lambda > 0$. There are in general three scale-free scalar theories: ϕ^4 model in $D = 4$ and ϕ^3 and ϕ^6 models in $D = 6, 3$ respectively. In this paper we only study ϕ^4 model in $D = 4$ though the main result of this paper can be simply generalized to the other two scalar models. The action in Euclidean space is

$$S[\phi] = \int d^4x \left(\frac{1}{2} \delta^{\mu\nu} \partial_\mu \phi \partial_\nu \phi - \frac{g}{4} \phi^4 \right) \tag{2}$$

where we assume $g > 0$. Consequently the potential $V(p) \sim -\phi^4$ and is not bounded from below. The Kronecker delta symbol $\delta^{\mu\nu}$ stands for the metric of flat Euclidean space. The corresponding equation of motion is a non-linear Laplace equation $\nabla^2 \phi + g\phi^3 = 0$, where $\nabla^2 = \delta^{\mu\nu} \partial_\mu \partial_\nu$. One can easily show that for $g > 0$, a solution of the non-linear Laplace equation is

$$\phi_0(x; \beta, a^\mu) = \sqrt{\frac{8}{g}} \frac{\beta}{\beta^2 + (x-a)^2}, \tag{3}$$

where $(x-a)^2 = \delta_{\mu\nu}(x-a)^\mu (x-a)^\nu$. β and a^μ are undetermined parameters describing the the size and location of ϕ_0. These moduli are consequences of symmetries of the action

i.e. invariance under rescaling and translation. The information geometry of the moduli space, given by Hitchin formula [9]

$$\mathscr{G}_{IJ} = \frac{1}{N}\int d^4x \mathscr{L}_0 \partial_I (\log \mathscr{L}_0)\, \partial_J (\log \mathscr{L}_0)\,, \tag{4}$$

is an Euclidean AdS$_5$ space (1). $N = \frac{4^3}{5}\int d^4x \mathscr{L}_0$ is a normalization constant and $\mathscr{L}_0 = \frac{g}{4}\phi_0^4$ is the Lagrangian density calculated at $\phi = \phi_0$. The moduli a^μ are present since the action is invariant under translation. The existence of β is the result of invariance under rescaling [11].

To my knowledge, the solution ϕ_0 is obtained for the first time by Fubini. He looked for a solution of the equation of motion "in which the vacuum expectation value of the field $\phi(x)$ is non-vanishing" [8]. He verified that this vacua is not invariant under the Poincare group but is invariant under the de Sitter group $O(3,1)$. Consequently by recasting the action in terms of new fields $\tilde{\phi} = \phi - \phi_0$ one expects to obtain, after some field redefinitions, a scalar theory in de Sitter background. In fact the action in terms of $\tilde{\phi}$ is,

$$S[\phi] = S[\phi_0] + S_{\text{free}}[\tilde{\phi}] + S_{\text{int}}[\tilde{\phi}], \tag{5}$$

where $S[\phi_0] = \int d^4x \mathscr{L}_0 = \frac{8\pi^2}{3g}$, and

$$S_{\text{free}}[\tilde{\phi}] = \int d^4x \left(\frac{1}{2}\delta^{\mu\nu}\partial_\mu\tilde{\phi}\partial_\nu\tilde{\phi} + \frac{1}{2}M^2(x)\tilde{\phi}^2\right), \tag{6}$$

in which,

$$M^2(x) = -3g\phi_0^2 = -24\frac{\beta^2}{(\beta^2+(x-a)^2)^2}. \tag{7}$$

These equations show that ϕ_0 is a metastable local minima of the action. This can also be verified explicitly by numerical analysis of action (2), see ref. [11]. Equation (6) can be used to show that the stability increases as $\beta \to \infty$. In fact if we calculate the variation of action at the stationary point $\phi_0(\beta)$ for different values of the moduli β_1 and β_2, under variation $\delta\phi$, from Eqs.(6,7) one verifies that,

$$\begin{aligned}\Delta S &= \delta S|_{\beta_1} - \delta S|_{\beta_2} \\ &\sim \int d^4x \left(\phi_0(\beta_2)^2 - \phi_0(\beta_1)^2\right)\delta\phi^2 + \mathscr{O}(\delta\phi^3).\end{aligned} \tag{8}$$

For simplicity we assume that $a_i^\mu = 0$, $i = 1,2$. Therefore ΔS is proportional to,

$$(\beta_1^2 - \beta_2^2)\int_0^\infty dx \frac{x^3(-x^4+\beta_1^2\beta_2^2)}{(\beta_1^2+x^2)^2(\beta_1^2+x^2)^2}\delta\phi^2. \tag{9}$$

For $\delta\phi$ with compact support, i.e. $\delta\phi = 0$ *if* $|x| > \sqrt{\beta_1\beta_2}$ the integral above is positive therefore $\Delta S \sim (\beta_1^2 - \beta_2^2)$. As far as ϕ_0 is a metastable local minima there exist $\delta\phi$ with compact support such that $\delta S|_{\beta_i} > 0$ $i = 1,2$. Consequently if $\beta_1 > \beta_2$ then $\delta S|_{\beta_1} > \delta S|_{\beta_2} > 0$. One can convince herself/himself that for some $\delta\phi$ one obtains $\delta S|_{\beta_2} < 0$ while $\delta S|_{\beta_1} > 0$. Consequently one concludes that there is a transition $\beta_2 \to \beta_1$ induced by say, thermal fluctuations. In addition the stability increases as $\beta \to \infty$.

The mass term in Eq.(6) can be interpreted as interaction with the background ϕ_0. Now recall that in general, by inserting $\tilde{\phi} = \sqrt{\Omega}\bar{\phi}$ and $\delta_{\mu\nu} = \Omega^{-1}g_{\mu\nu}$ in the action $S[\tilde{\phi}] = \int d^4x \frac{1}{2}\delta^{\mu\nu}\partial_\mu\tilde{\phi}\partial_\nu\tilde{\phi}$, one obtains,

$$S[\tilde{\phi}] = \int d^4x\sqrt{g}\left(\frac{1}{2}g^{\mu\nu}\partial_\mu\bar{\phi}\partial_\nu\bar{\phi} + \frac{1}{2}\xi R\bar{\phi}^2\right), \tag{10}$$

i.e. a scalar theory on conformally flat background given by the metric $g_{\mu\nu} = \Omega\delta_{\mu\nu}$ in which $\Omega > 0$ is an arbitrary $\mathscr{C}^\infty$ function. R is the scalar curvature of the background and $\xi = \frac{1}{6}$ is the conformal coupling constant. For details see [14] or appendix C of [7]. Thus, defining $\bar{\phi} = \Omega^{\frac{-1}{2}}\tilde{\phi}$, one can show that $S_{\text{free}}[\tilde{\phi}]$ given in Eq.(6) is the action of the scalar field $\bar{\phi}$ on some conformally flat background,

$$\begin{aligned}S_{\text{free}}[\phi] = \int d^4x\sqrt{|g|}\Big(&\frac{1}{2}g^{\mu\nu}\partial_\mu\phi\,\partial_\nu\phi \\ &+\frac{1}{2}(\xi R + m^2)\phi^2\Big).\end{aligned} \tag{11}$$

with metric

$$g_{\mu\nu} = \Omega\delta_{\mu\nu}, \qquad \Omega = \frac{M^2(x)}{m^2}, \tag{12}$$

where m^2 is the mass of $\bar{\phi}$ (undetermined) and $M^2(x)$ is given in Eq.(7). This result is surprising as one can show that the Ricci tensor $R_{\mu\nu} = \Lambda g_{\mu\nu}$, where $\Lambda = -\frac{m^2}{2} > 0$ as far as $\Omega > 0$. Consequently $\bar{\phi}$ lives in a four dimensional de Sitter space which scalar curvature $R = -2m^2$. The interacting part of the action, $S_{\text{int}}[\tilde{\phi}] = \int d^4x\sqrt{|g_{\mu\nu}|}\mathscr{L}_{\text{int}}$ is well-defined in terms of $\bar{\phi}$ on the corresponding dS$_4$:

$$\mathscr{L}_{\text{int}} = -g\sqrt{\frac{-m^2}{3g}}\bar{\phi}^3 - \frac{g}{4}\bar{\phi}^4. \tag{13}$$

Interestingly after a shift of the scalar field $\bar{\phi} \to \bar{\phi} - \sqrt{\frac{-m^2}{3g}}$ the action (5) can be written in the dS$_4$ as follows:

$$\begin{aligned}S[\bar{\phi}] = \int d^4x\sqrt{|g|}\Big(&\frac{1}{2}g^{\mu\nu}\partial_\mu\bar{\phi}\,\partial_\nu\bar{\phi} \\ &+\frac{1}{2}\xi R\,\bar{\phi}^2 - \frac{g}{4}\bar{\phi}^4\Big).\end{aligned} \tag{14}$$

This is a scalar theory in a de Sitter background with reversed Mexican hat potential. In a similar way, by recasting the critical scalar theory minimally coupled to $U(1)$ gauge field in terms of fluctuations around the classical solution $\phi = \phi_0$ and $A_\mu = 0$, one verifies that the action

$$S = \int d^4x\left(|D_\mu\phi|^2 - \frac{g}{2}|\phi|^4\right) + S_A, \tag{15}$$

is equivalent to

$$S = S[\phi_0] + S[\bar{\phi}, A_\mu] + S_A, \tag{16}$$

where

$$S[\bar{\phi}, A_\mu] = \int d^4x\sqrt{g}\left(\frac{1}{2}g^{\mu\nu}D_\mu\bar{\phi}D_\nu\bar{\phi}^* + V(\bar{\phi})\right), \tag{17}$$

$V(\bar{\phi}) = \frac{1}{2}\xi R\left|\bar{\phi}\right|^2 - \frac{g}{4}\left|\bar{\phi}\right|^4$ and S_A is the Kinetic term for the gauge field,

$$\begin{aligned} S_A &= -\frac{1}{4}\int d^4x F_{\mu\nu}F_{\rho\sigma}\delta^{\rho\mu}\delta^{\sigma\nu} \\ &= -\frac{1}{4}\int d^4x\sqrt{g}g^{\mu\rho}g^{\nu\sigma}F_{\mu\nu}F_{\rho\sigma}. \end{aligned} \tag{18}$$

$F_{\mu\nu}$ in the first equality above is the field strength in Minkowski spacetime. In the second equality $F_{\mu\nu}$ should be understood as the field strength on the de Sitter space [11]. It should be noted that under the conformal transformation $g_{\mu\nu} \to \Omega g_{\mu\nu}$, in four dimensions $A_\mu \to A_\mu$.

3 The critical scalar theory in Minkowski spacetime

The critical scalar theory in four dimensional Minkowski spacetime is given by the action

$$S[\phi] = \int d^4x\left(\frac{1}{2}\eta^{\mu\nu}\partial_\mu\phi\partial_\nu\phi + \frac{g}{4}\phi^4\right), \tag{19}$$

where $\eta_{\mu\nu} = (+,-,-,-)$ and $g > 0$. The equation of motion is a non-linear wave equation $\eta^\mu\partial_\mu\partial_\nu\phi - g\phi^3 = 0$ which has the solution

$$\phi_0 = \sqrt{\frac{8}{g}}\frac{\beta}{\beta^2 - (t-a^0)^2 + |\vec{x}-\vec{a}|^2}, \tag{20}$$

where $\vec{x} \in \mathbf{R}^3$. Here on we assume $a^\mu = 0$ for simplicity. ϕ_0 is singular on the hyperbola $t^2 = x^2 + \beta^2$ and we define its distance to an observer located on the origin to be given by β. The Hamiltonian density $\mathscr{H}$ corresponding to ϕ_0, is,

$$\mathscr{H} = \frac{16\beta^2}{g}\frac{t^2+x^2-\beta^2}{(-t^2+x^2+\beta^2)^4} \tag{21}$$

which tends to infinity in the vicinity of the singularity. As is explained in the introduction, using the results of section 2 and the arguments after Eq.(9), we now that the most stable ϕ_0 is the zero-sized one, corresponding to $\beta \to \infty$. Therefore the singularity is safe when the scalar theory is coupled to gravity. For $t < \beta$ one can calculate, say, the total vacuum energy $H = \int d^3x\mathscr{H}$ corresponding to ϕ_0 which is surprisingly vanishing, $H = 0$. Repeating the calculations of section 2 one verifies that observers located at the origin of the Minkowski spacetime observe a de Sitter space given by the conformally flat metric,

$$ds^2 = \frac{12\beta^2}{\Lambda}\frac{1}{(\beta^2 - t^2 + x^2)^2}(-dt^2 + d\vec{x}^2), \tag{22}$$

where $\Lambda > 0$ is the cosmological constant. This metric can be obtained using Eq.(12) after a Wick rotation $t \to it$. We use a different set of coordinates in order to describe the observed de Sitter space with FRW metric to see whether it is open, closed or flat. Defining, coordinates u, ρ and z_i, $i = 1,2,3$ by the relations $z_i^2 = 1$, $t = u\cosh\rho$ and $x_i = u\sinh\rho z_i$ useful to describe the timelike region $t > |\vec{x}|$, one obtains,

$$\begin{aligned} ds^2 = &\frac{12\beta^2}{\Lambda}\frac{1}{(\beta^2-u^2)^2} \\ &\times\left(-du^2 + u^2\left(d\rho^2 + \sinh^2\rho\, dz_i^2\right)\right). \end{aligned} \tag{23}$$

we define a time coordinate τ by the relation $d\tau = \left(\beta^2 - u^2\right)^{-1} du$. Thus one obtains,

$$\begin{aligned} ds^2 = \frac{12\beta^2}{\Lambda}\Bigg[&-d\tau^2 \\ &+ \frac{\sinh^2(2\beta\tau)}{4\beta^2}\left(d\rho^2 + \sinh^2\rho\, dz_i^2\right)\Bigg]. \end{aligned} \tag{24}$$

One can call the region $u < \beta$ which can be observed by observers located on the origin the south pole and the $u > \beta$ region the north pole, a known terminology in de Sitter geometry. The south pole and north pole in our model are separated by the horizon located at $u = \beta$, i.e the singularity of ϕ_0. By normalizing τ by the normalization factor $\sqrt{\frac{12}{\Lambda}}\beta$ and defining a new coordinate $r = \sinh\rho$, one at the end of the day obtains,

$$ds^2 = -d\tau^2 + a(\tau)^2\left(\frac{dr^2}{1+r^2} + r^2 dz_i^2\right), \tag{25}$$

in which $a(\tau) = \sqrt{\frac{3}{\Lambda}}\sinh\sqrt{\frac{\Lambda}{3}}\tau$. This is the Robertson-Walker metric for open de Sitter universe. One can easily calculate the energy density ρ and the pressure p of the cosmological stuff corresponding to ϕ_0 using the Friedmann equations for the open universe,

$$\begin{aligned} \left(\frac{\dot{a}}{a}\right)^2 &= \frac{8\pi G}{3}\rho + \frac{1}{a^2}, \\ \frac{\ddot{a}}{a} &= -\frac{4\pi G}{3}(\rho + 3p). \end{aligned} \tag{26}$$

One verifies that p and ρ satisfy the equation of state for the cosmological constant $\rho = -p = \Lambda$ ($8\pi G = 1$).

References

1. D.N. Spergel et al., *Astrophys. J. Suppl.* **148** (2003) 175, DOI: 10.1086/377226, arXiv: astro-ph/0302209.
2. J.R. Gott, Nature 295 (1982) 304, DOI: 10.1038/295304a0.
3. P.J. Peebles, D.N. Schramm, E.L. Turner and R.G. Kron, Nature 352 (1991) 769.

4. S. Kachru, R. Kallosh, A. Linde and S.P. Trivedi, *Phys. Rev. D* **68** (2003) 046005, DOI: 10.1103/PhysRevD.68.046005, arXiv: hep-th/0301240.
5. L. Susskind, *The Anthropic Landscape of String Theory*, arXiv: hep-th/0302219.
6. S.B. Giddings, S. Kachru and J. Polchinski, *Phys. Rev. D* **66** (2002) 106006, DOI: 10.1103/PhysRevD.66.106006, arXiv: hep-th/0105097.
7. F. Loran, Phys. Rev. D 71 (2005) 126003, DOI: 10.1103/PhysRevD.71.126003, hep-th/0501189.
8. S. Fubini, Nuovo Cim. A34 (1976) 521.
9. N. J. Hitchin, *The Geometry and Topology of Moduli Spaces* in *Global Geometry and Mathematical Physics*, (Springer, Heidelberg, 1988) 1–48;
   R. Britto, B. Feng, O. Lunin and S. J. Rey, *Phys. Rev. D* **69** (2004) 126004, DOI: 10.1103/PhysRevD.69.126004, arXiv: hep-th/0311275;
   S. Parvizi, *Mod. Phys. Lett. A* **17** (2002) 341–354, DOI: 10.1142/S0217732302006568, arXiv: hep-th/0202025.
10. M. Blau, K. S. Narain and G. Thompson, *Instantons, the Information Metric, and the AdS/CFT Correspondence*, arXiv: hep-th/0108122.
11. F. Loran and E. Bavarsad, "Metastable de Sitter Vacua from Critical Scalar Theory," *Trans. Theor. Math. Phys.* (2026), 54–58. DOI: 10.30511/ttmp.2026.2089573.1078, .
12. S.R. Coleman, Phys. Rev. D15 (1977) 2929, DOI: 10.1103/PhysRevD.15.2929.
13. A.R. Frey, M. Lippert and B. Williams, *Phys. Rev. D* **68** (2003) 046008, DOI: 10.1103/PhysRevD.68.046008, arXiv: hep-th/0305018.
14. T. Jacobson, *Introduction to Quantum Fields in Curved Spacetime and the Hawking Effect*, gr-qc/0308048.

TTMP vol 3 (2), 2026
doi: 10.30511/TTMP.2026.2091664.1080

Transactions in Theoretical and Mathematical Physics

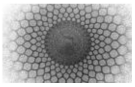

The Second-Order Basis for Homogeneous Solutions of Compatible Higher Order Linear ODEs with Varying Coefficients

Gunawan Nugroho[1a], **Totok R. Biyanto**[1]

[1] Departement of Engineering Physics, Institut Teknologi Sepuluh Nopember Kampus ITS Sukolilo, Surabaya, Indonesia 60111

Received: 15 May 2026 / Accepted: 21 May 2026 / Published: 29 May 2026

Abstract This research presents a reduction and reconstruction study for third and fourth order linear ordinary differential equations with variable coefficients, including equations with nonzero dependent variable terms. A compatible higher order equation is reduced to a second order ODE and then is solved analytically to produce the homogeneous solution required by variation of parameters and the Wronskian. Once this homogeneous solution is found, the systematic general solution follows from the classical variation of parameters, represented here by equation (9d). The work therefore aims to pierce the main difficulty of variable coefficient problems: finding an analytical homogeneous solution for the linear compatible ODE with varying coefficients. Validation is performed on Airy, Bessel, Legendre, and Weber type models, including induced third and fourth order equations and beyond special functions coefficients. Numerical comparisons with classical special functions show agreement at round off scale.

Keywords: Variable-coefficient ordinary differential equations; reduction of order; analytical solution; integrating factor; special functions

1 Introduction

Linear ODEs with variable coefficients are foundational in mathematical physics, engineering dynamics, wave propagation, elasticity, quantum mechanics, and stability theory. Classical theory established that variable coefficients, singular points, and boundary behavior fundamentally complicate solution structures beyond constant-coefficient cases [1, 2]. Thus, the special functions such as Airy, Bessel, Legendre, and parabolic-cylinder functions arise naturally from second-order variable-coefficient equations and continue to serve as benchmarks for analytical and numerical methods [3, 4].

Despite extensive developments in Frobenius series, WKB approximations, contour-integral representations, variation of parameters, and transformation-based techniques, systematic approaches that reduce higher-order variable-coefficient ODEs to solvable lower-order forms remain of strong interest. Recent studies have advanced generalized integrating factors for second- and third-order equations [5–7]. Gadella and Lara emphasized that exact solutions for variable coefficient systems are generally difficult except for special structures [8]. Recent applied mathematics treatments continue to introduce Wronskians, Cauchy problems, first and second order linear equations, and Euler type or special equations as the main analytical tools [9]. Open educational resources published in recent years also continue to present higher order equations through Wronskians, superposition, variation of parameters, and reduction of order, showing that the topic remains central in current teaching and research practice [10].

The analytical bottleneck can be stated very clearly: the general solution is systematic if a fundamental homogeneous pair is known. The Wronskian and variation of parameters then produce a particular solution and complete the solution space. However, finding even one nontrivial homogeneous solution for a variable-coefficient equation is the main difficulty. This observation motivates the present work on variable-coefficient linear ODEs, which constructs a correct homogeneous solution so that variation of parameters and reduction of order become systematic and classical. In this sense, the proposed approach is complementary to the standard methodology: first reduce a compatible higher-order equation to a second-order equation, then solve the second-order ODE analytically, and finally use the Wronskian and variation of parameters to establish the general solution.

[a]gunawan@ep.its.ac.id

This paper contributes a structured reduction-of-order method for compatible third- and fourth-order linear ODEs. The method transforms the original equation into a reduced form in which a derivative of the dependent variable satisfies a second-order variable-coefficient ODE. The reduced second-order equation is solved analytically, followed by inverse transformations to reconstruct the original solution. To validate the framework, the paper applies the reduction to Airy, Bessel, Legendre, and Weber equations of higher-order type. These functions are classical enough to provide exact benchmark solutions, while remaining sufficiently rich to test variable-coefficient behavior. Additional examples involving non-special variable terms are also considered, demonstrating that the applicability of the method extends beyond constructive special-function settings.

2 The Mathematical Formulations

2.1 Reduction of 3rd Order ODE

Firstly, we would like to state that the written symbols and coefficients are freely chosen for convenience and the reader should not be confused by perceiving that each subsection has its own variables and coefficients. Consider a non-homogeneous third-order linear differential equation with variable coefficients,

$$y_{xxx}+a_1y_{xx}+a_2y_x+a_3y=a_4, \tag{1a}$$

Let $a_1=b_1+\frac{a_{5x}}{a_5}$, then equation (1a) can be rewritten as

$$\frac{1}{a_5}(a_5y_{xx})_x+b_1y_{xx}+a_2y_x+a_3y=a_4. \tag{1b}$$

Also take $a_2=b_2+b_1\frac{a_{6x}}{a_6}$, thus the following relation is obtained,

$$\frac{1}{a_5}(a_5y_{xx})_x+\frac{b_1}{a_6}(a_6y_x)_x+b_2y_x+a_3y=a_4. \tag{1c}$$

Multiply by an arbitrary function α to generate,

$$\frac{\alpha}{a_5}(a_5y_{xx})_x+\frac{\alpha b_1}{a_6}(a_6y_x)_x+\alpha b_2y_x+\alpha a_3y=\alpha a_4. \tag{1d}$$

Suppose that the following expression is satisfied,

$$\alpha_x b_2=\alpha a_3, \qquad \alpha=C_1e^{\int\frac{a_3}{b_2}dx}. \tag{1e}$$

Let $C_1=1$, equation (1d) is rewritten as

$$\frac{\alpha}{a_5}(a_5y_{xx})_x+\frac{\alpha b_1}{a_6}(a_6y_x)_x+b_2\left(e^{\int\frac{a_3}{b_2}dx}y\right)_x=\alpha a_4. \tag{1f}$$

Suppose that

$$e^{\int\frac{a_3}{b_2}dx}y=u, \qquad y=ue^{-\int\frac{a_3}{b_2}dx}. \tag{2a}$$

Therefore, equation (1f) can be expanded as

$$\begin{aligned}&\frac{\alpha}{a_5}\left\{a_5\left[u_{xx}e^{-\int\frac{a_3}{b_2}dx}+2u_x\left(-\frac{a_3}{b_2}\right)e^{-\int\frac{a_3}{b_2}dx}\right.\right.\\&\left.\left.+u\left(-\frac{a_3}{b_2}\right)_x e^{-\int\frac{a_3}{b_2}dx}+u\left(-\frac{a_3}{b_2}\right)^2e^{-\int\frac{a_3}{b_2}dx}\right]\right\}_x\\&+\frac{\alpha b_1}{a_6}\left\{a_6\left[u_xe^{-\int\frac{a_3}{b_2}dx}+u\left(-\frac{a_3}{b_2}\right)e^{-\int\frac{a_3}{b_2}dx}\right]\right\}_x\\&+b_2u_x=\alpha a_4.\end{aligned} \tag{2b}$$

Assume that

$$\begin{aligned}&\frac{\alpha}{a_5}\left[a_5e^{-\int\frac{a_3}{b_2}dx}\left(\left(-\frac{a_3}{b_2}\right)^2+\left(-\frac{a_3}{b_2}\right)_x\right)\right]_x\\&+\frac{\alpha b_1}{a_6}\left[a_6\left(-\frac{a_3}{b_2}\right)e^{-\int\frac{a_3}{b_2}dx}\right]_x=0.\end{aligned} \tag{2c}$$

Now assume that b_2 is given, then $\frac{a_{6x}}{a_6}$ can be determined from (2c) as

$$\frac{a_{6x}}{a_6}=\frac{f_6\frac{a_{5x}}{a_5}+b_1f_7+f_8}{b_1f_9}. \tag{2d}$$

Substituting into $a_2=b_2+b_1\frac{a_{6x}}{a_6}$ to give the expression of b_1 as a function of $\frac{a_{5x}}{a_5}$. Performing the resulting expression into $a_1=b_1+\frac{a_{5x}}{a_5}$ to generate a_5. Therefore, equation (1a) is reduced into $u_{xxx}+a_7u_{xx}+a_8u_x=a_9$. Let $u_x=v$, thus the above equation can be transformed to the second-order ODE,

$$g_{xx}+a_7g_x+a_8g=a_9, \quad \text{or} \quad g_{xx}+p(x)g_x+r(x)g=0. \tag{2e}$$

This establishes that the original third-order equation is reduced to a second-order equation in $v(x)$, provided the coefficient decomposition $(a_1,a_2,a_3)\to(a_7,a_8,a_9)$ exists.

2.2 Reduction of 4th Order ODE

Consider a non-homogeneous fourth-order linear differential equation with variable coefficients below,

$$y_{xxxx}+a_1y_{xxx}+a_2y_{xx}+a_3y_x+a_4y=a_5. \tag{3a}$$

Suppose that $a_1=b_1+\frac{a_{6x}}{a_6}$, and $a_2=b_2+b_1\frac{a_{7x}}{a_7}$, and $a_3=b_3+b_2\frac{a_{8x}}{a_8}$, equation (3a) becomes

$$\begin{aligned}&\frac{1}{a_6}(a_6y_{xxx})_x+\frac{b_1}{a_7}(a_7y_{xx})_x\\&+\frac{b_2}{a_8}(a_8y_x)_x+b_3y_x+a_4y=a_5.\end{aligned} \tag{3b}$$

Multiplying by an arbitrary function α to give $\frac{\alpha}{a_6}(a_6y_{xxx})_x + \frac{\alpha b_1}{a_7}(a_7y_{xx})_x + \frac{\alpha b_2}{a_8}(a_8y_x)_x + \alpha b_3 y_x + \alpha a_4 y = a_5$.
Take the following relation,

$$\alpha_x b_3 = \alpha a_4, \qquad \alpha = C_1 e^{\int \frac{a_4}{b_3}\,dx}. \tag{3c}$$

Equation (3c) is transformed as

$$\begin{aligned}\frac{\alpha}{a_6}(a_6y_{xxx})_x + \frac{\alpha b_1}{a_7}(a_7y_{xx})_x + \frac{\alpha b_2}{a_8}(a_8y_x)_x \\ + b_3\left(e^{\int \frac{a_4}{b_3}\,dx} y\right)_x = \alpha a_5.\end{aligned} \tag{3d}$$

Let us assume that

$$e^{\int \frac{a_4}{b_3}\,dx} y = u, \qquad y = u e^{-\int \frac{a_4}{b_3}\,dx}. \tag{4a}$$

Expanding equation (3d) as

$$\begin{aligned}&\frac{\alpha}{a_6}\left\{a_6\left[u_{xxx}E + 3u_{xx}\left(-\frac{a_4}{b_3}\right)E + 3u_x\left(-\frac{a_4}{b_3}\right)_x E\right.\right. \\ &\quad + 3u_x\left(-\frac{a_4}{b_3}\right)^2 E + u\left(-\frac{a_4}{b_3}\right)_{xx} E \\ &\quad \left.\left. + 3u\left(-\frac{a_4}{b_3}\right)_x\left(-\frac{a_4}{b_3}\right)E + u\left(-\frac{a_4}{b_3}\right)^3 E\right]\right\}_x \\ &+ \frac{\alpha b_1}{a_7}\left\{a_7\left[u_{xx}E + 2u_x\left(-\frac{a_4}{b_3}\right)E + u\left(-\frac{a_4}{b_3}\right)_x E\right.\right. \\ &\quad \left.\left. + u\left(-\frac{a_4}{b_3}\right)^2 E\right]\right\}_x \\ &+ \frac{\alpha b_2}{a_8}\left\{a_8\left[u_x E + u\left(-\frac{a_4}{b_3}\right)E\right]\right\}_x + b_3 u_x = \alpha a_5.\end{aligned} \tag{4b}$$

where $E = e^{-\int \frac{a_4}{b_3}\,dx}$. Performing the following relation,

$$\begin{aligned}&\frac{\alpha}{a_6}\left[a_6\left(-\frac{a_4}{b_3}\right)_{xx} E + 3a_6\left(-\frac{a_4}{b_3}\right)_x\left(-\frac{a_4}{b_3}\right)E\right. \\ &\qquad \left. + a_6\left(-\frac{a_4}{b_3}\right)^3 E\right]_x \\ &+ \frac{\alpha b_1}{a_7}\left[a_7\left(-\frac{a_4}{b_3}\right)^2 E + a_7\left(-\frac{a_4}{b_3}\right)_x E\right]_x \\ &\qquad + \frac{\alpha b_2}{a_8}\left[a_8\left(-\frac{a_4}{b_3}\right)E\right]_x = 0.\end{aligned} \tag{4c}$$

Suppose that b_3 and a_8 are given, then $\frac{a_{7x}}{a_7}$ can be determined from (4c) as

$$\frac{a_{7x}}{a_7} = \frac{f_{10}\frac{a_{6x}}{a_6} + b_1 f_{11} + f_{12}}{b_1 f_{13}}. \tag{4d}$$

Substituting (4d) into $a_2 = b_2 + b_1\frac{a_{7x}}{a_7}$ to give b_1 as a function of $\frac{a_{6x}}{a_6}$. The next step is implementing into $a_1 = b_1 + \frac{a_{6x}}{a_6}$ to produce a_6. Therefore, the fourth-order equation is reduced into $u_{xxxx} + a_9u_{xxx} + a_{10}u_{xx} + a_{11}u_x = a_{12}$.

Let $u_x = v$, thus the above equation can be transformed to the third-order equation,

$$g_{xxx} + a_9 g_{xx} + a_{10} g_x + a_{11} g = a_{12}. \tag{4e}$$

Implementing the third-order reduction into (4e), both third- and fourth-order equations are systematically reduced to the same second-order structure, provided the auxiliary coefficients satisfy compatibility relations.

2.3 Analytical Solution of 2nd Order ODE with Varying Coefficients

Consider the 2nd order ODE equation with variable coefficients as follows,

$$A_{xx} + f_1(x)A_x + f_2(x)A = 0. \tag{5a}$$

Let $A = wB$, then

$$B_{xx} + \left(2\frac{w_x}{w} + f_1\right)B_x + \left(\frac{w_{xx} + f_1 w_x + f_2 w}{w}\right)B = 0. \tag{5b}$$

Take $2\frac{w_x}{w} + f_1 = a_1 = 0$, then w is determined by

$$w = e^{-\frac{1}{2}\int f_1\,dx}. \tag{5c}$$

and equation (5a) is rewritten as

$$B_{xx} + a_2 B = 0, \tag{5d}$$

where $a_2 = \frac{w_{xx} + f_1 w_x + f_2 w}{w}$.

Let $B = (yZ)_x$, equation (5d) becomes

$$(yZ)_{xxx} + a_2(yZ)_x = 0,$$

or

$$yZ_{xxx} + 3y_xZ_{xx} + 3y_{xx}Z_x + y_{xxx}Z + a_2yZ_x + a_2y_xZ = 0, \tag{6a}$$

or

$$yZ_{xxx} + 3y_xZ_{xx} + (3y_{xx} + a_2y)Z_x + (y_{xxx} + a_2y_x)Z = 0.$$

Suppose that $3y_x = b_1 + y\frac{a_{3x}}{a_3}$, $3y_{xx} + a_2y = b_2 + b_1\frac{a_{4x}}{a_4}$, equation (6a) is rewritten as

$$\frac{y}{a_3}(a_3Z_{xx})_x + \frac{b_1}{a_4}(a_4Z_x)_x + b_2Z_x + \gamma Z = 0, \tag{6b}$$

where $\gamma = y_{xxx} + a_2 y_x$. Introducing the integrating factor $\beta = e^{\int \frac{\gamma}{b_2} dx}$, to give

$$\frac{\beta y}{a_3}(a_3 Z_{xx})_x + \frac{\beta b_1}{a_4}(a_4 Z_x)_x + b_2(\beta Z)_x = 0,$$

or

$$\begin{aligned}
&\frac{\beta y}{a_3}\left\{ a_3\left[e^{-\int \frac{\gamma}{b_2} dx} U_{xx} + 2\left(-\frac{\gamma}{b_2}\right) e^{-\int \frac{\gamma}{b_2} dx} U_x \right.\right. \\
&\left.\left. + \left(-\frac{\gamma}{b_2}\right)^2 e^{-\int \frac{\gamma}{b_2} dx} U + \left(-\frac{\gamma}{b_2}\right)_x e^{-\int \frac{\gamma}{b_2} dx} U\right]\right\}_x \\
&+ \frac{\beta b_1}{a_4}\left\{ a_4\left[e^{-\int \frac{\gamma}{b_2} dx} U_x + \left(-\frac{\gamma}{b_2}\right) e^{-\int \frac{\gamma}{b_2} dx} U\right]\right\}_x \\
&+ b_2 U_x = 0.
\end{aligned} \tag{6c}$$

with $U = \beta Z$. Set the following condition,

$$\frac{\beta y}{a_3}\left[a_3 \chi^2 e^{\int \chi dx} + a_3 \chi_x e^{\int \chi dx}\right]_x + \frac{\beta b_1}{a_4}\left[a_4 \chi e^{\int \chi dx}\right]_x = 0. \tag{6d}$$

Expanding (6d),

$$\begin{aligned}
&\left[\frac{\beta y a_{3x}}{a_3}\chi e^{\int \chi dx} + \beta y \chi^3 e^{\int \chi dx} + 3\beta y \chi \chi_x e^{\int \chi dx}\right] \\
&+ \left[\frac{\beta y a_{3x}}{a_3}\chi_x e^{\int \chi dx} + \beta y \chi_{xx} e^{\int \chi dx}\right] \\
&+ \left[\frac{\beta b_1 a_{4x}}{a_4}\chi e^{\int \chi dx} + \beta b_1 \chi_x e^{\int \chi dx} + \beta b_1 \chi^2 e^{\int \chi dx}\right] \\
&= 0,
\end{aligned} \tag{1}$$

where $\chi(x) = -\frac{\gamma}{b_2}$. Recalling the definition of β, equation (6d) is rewritten as

$$\begin{aligned}
&\left[\frac{y a_{3x}}{a_3}\chi + y\chi^3 + 3y\chi\chi_x + \frac{y a_{3x}}{a_3}\chi_x + y\chi_{xx}\right] \\
&\qquad + \left[\frac{b_1 a_{4x}}{a_4}\chi + b_1\chi_x + b_1\chi^2\right] = 0.
\end{aligned} \tag{6e}$$

Equation (6c) is then defined by

$$\begin{aligned}
&\frac{\beta y}{a_3}\left[a_3 e^{\int \chi dx} U_{xxx} + a_3 \chi e^{\int \chi dx} U_{xx} + a_{3x} e^{\int \chi dx} U_{xx} \right. \\
&+ 2a_3 \chi e^{\int \chi dx} U_{xx} + 2a_3 \chi^2 e^{\int \chi dx} U_x + 2a_{3x}\chi e^{\int \chi dx} U_x \\
&\left. + a_3 \chi^2 e^{\int \chi dx} U_x + a_3 \chi_x e^{\int \chi dx} U_x\right] \\
&+ \frac{\beta b_1}{a_4}\left[a_4 e^{\int \chi dx} U_{xx} + a_4 \chi e^{\int \chi dx} U_x \right. \\
&\qquad \left. + a_{4x} e^{\int \chi dx} U_x + a_4 \chi e^{\int \chi dx} U_x\right] \\
&+ b_2 U_x + \frac{\beta y}{a_3}\left[a_3 \chi^2 e^{\int \chi dx} U + a_3 \chi_x e^{\int \chi dx} U\right]_x \\
&+ \frac{\beta b_1}{a_4}\left[a_4 \chi e^{\int \chi dx} U\right]_x U = 0.
\end{aligned} \tag{7a}$$

Recalling the definition of β, equation (7a) is rewritten as

$$\begin{aligned}
&y U_{xxx} + \left[3y\chi + \frac{y a_{3x}}{a_3} + b_1\right] U_{xx} \\
&+ \left[3y\chi^2 + 2\frac{y a_{3x}}{a_3}\chi + y\chi_x + 2b_1\chi + \frac{b_1 a_{4x}}{a_4} + b_2\right] U_x \\
&= 0.
\end{aligned} \tag{7b}$$

Substituting $b_1 = 3y_x - y\frac{a_{3x}}{a_3}$, $b_1 \frac{a_{4x}}{a_4} = 3y_{xx} + a_2 y - b_2$, into (6e),

$$\begin{aligned}
&y U_{xxx} + \left[3y\chi + 3y_x\right] U_{xx} \\
&\quad + \left[3y\chi^2 + y\chi_x + 6y_x\chi + 3y_{xx} + a_2 y\right] U_x = 0,
\end{aligned}$$

or

$$\begin{aligned}
&U_{xxx} + \left[3\chi + 3\frac{y_x}{y}\right] U_{xx} \\
&\quad + \left[3\chi^2 + \chi_x + 6\frac{y_x}{y}\chi + 3\frac{y_{xx}}{y} + a_2\right] U_x = 0.
\end{aligned} \tag{7c}$$

Take the following condition, $\left[3\chi + 3\frac{y_x}{y}\right]_x = \left[3\chi^2 + \chi_x + 6\frac{y_x}{y}\chi + 3\frac{y_{xx}}{y} + a_2\right]$. The y- and b_2-dependent terms can be separated as

$$-3\left(\frac{y_x}{y}\right)^2 - a_2 = 3\chi^2 - 2\chi_x + 6\frac{y_x}{y}\chi = 0. \tag{8a}$$

Thus, each solution will be

$$y = C_1 e^{-\int \sqrt{\frac{1}{3}a_2} dx}, \qquad \chi = -\frac{2}{3}\frac{y^3}{\int y^3 dx + C_2}. \tag{8b}$$

Furthermore, equation (6e) is performed into $3y_x = b_1 + y\frac{a_{3x}}{a_3}$, as follows,

$$b_1\left(-\chi - \frac{a_{4x}}{a_4} + 1\right) = 3y_x + y\chi^2 + 3y\chi_x - 3y_x\chi_x\chi^{-1} - y\chi_{xx}\chi^{-1}. \tag{8c}$$

Then, substitute equation (8c) into $3y_{xx} + a_2 y = b_2 + b_1\frac{a_{4x}}{a_4}$ to form the equation for a_4,

$$(3y_{xx} + a_2 y - b_2)\left(-\chi - \frac{a_{4x}}{a_4} + 1\right) = \frac{a_{4x}}{a_4}\left[3y_x + y\chi^2 + 3y\chi_x - 3y_x\chi_x\chi^{-1} - y\chi_{xx}\chi^{-1}\right]. \tag{8d}$$

and the solution can be directly found.

After establishing the coefficient relations, now we move to equation (7d), which is simplified as

$$U_{xx} + \left[3\chi + 3\frac{y_x}{y}\right]U_x = C_3. \tag{9a}$$

and the solution for U and A are

$$U = C_3\int y^{-3}e^{-3\int\chi\,dx}\left[\int\left(y^3e^{3\int\chi\,dx}\right)dx\right]dx + C_4\int\left(y^{-3}e^{-3\int\chi\,dx}\right)dx + C_5. \tag{9b}$$

and

$$A = wB = w(yZ)_x = w\left(ye^{\int\chi\,dx}U\right)_x. \tag{9c}$$

where w and U are defined by (5c) and (9b). Thus the general solution for A with forcing function f_3 is

$$A_h^2A_{p,xx} + 2A_hA_{h,x}A_{p,x} + f_1A_h^2A_{p,x} = A_hf_3,$$

or

$$A = A_hA_p = A_h\left[\int\frac{1}{A_h^2}e^{-\int f_1\,dx}\left(\int A_hf_3e^{\int f_1\,dx}dx\right)dx\right] + C_6A_h\left(\int\frac{1}{A_h^2}e^{-\int f_1\,dx}dx\right) + C_7A_h. \tag{9d}$$

Note that the second term of (9d) is exactly the second homogeneous solution used by variation of parameters, which in this method appears as a consequence of generating the general solution.

3 Validation Against Various Physical and Engineering Models

To establish the quantitative reliability of the reduction and reconstruction methods, the proposed analytical solutions are benchmarked against high-accuracy direct numerical integration of the original higher-order equations. The reference solution $y_{\text{ref}}(x)$ is obtained by direct integration of the full third- or fourth-order ODE using the DOP853 algorithm [12], implemented via `scipy.integrate.solve_ivp` [11]. DOP853 is an explicit eighth-order Runge–Kutta method with seventh-order dense output, widely adopted for non-stiff high-precision problems due to its adaptive step-size control, embedded error estimation, and robust handling of smooth variable coefficients.

3.1 Airy Equation (Quantum Tunneling & Wave Propagation)

The reduced mechanism $A_{xx} - xA = 0$ models quantum wavefunctions near classical turning points and diffraction caustics. Applying the framework with $f_1 = 0$, $f_2 = -x$, yields $w = 1$, $a_2 = -x$. The compatibility conditions select $y(x) = \text{Ai}(x)$, and Eqs. (9a)–(9c) reconstruct the homogeneous solution. The C_6 term in (9d) generates $\text{Bi}(x)$ via $A_2 = A_h\int A_h^{-2}\,dx$. Maximum absolute error over $[-2, 2]$: 6.74×10^{-13}.

3.2 Bessel Equation (Cylindrical Waveguides & Heat Transfer)

The reduced equation $A_{xx} + x^{-1}A_x + \left(1 - \nu^2x^{-2}\right)A = 0$, $(\nu = 0.7)$, governs radial modes in cylindrical coordinates. Normalization yields $w = x^{-1/2}$, transforming the equation to a Schrödinger-type form with potential $a_2(x) = 1 + \frac{\frac{1}{4}-\nu^2}{x^2}$. The reconstruction recovers $J_\nu(x)$ as A_h, and variation of parameters yields $Y_\nu(x)$. Error over $[0.5, 2]$: 5.33×10^{-15}.

3.3 Legendre Equation (Potential Theory & Spherical Harmonics)

The reduced equation $(1 - x^2)A_{xx} - 2xA_x + \ell(\ell + 1)A = 0$, $\ell = 7$, exhibits endpoint singularities at $x = \pm 1$. The normalization factor $w = (1 - x^2)^{-1/2}$ absorbs the f_1 singularity, yielding $B_{xx} + a_2(x)B = 0$, with $a_2(x) = \frac{56}{1-x^2} + \frac{1}{(1-x^2)^2}$. The reconstruction isolates the polynomial branch $P_7(x)$, while the quadrature integral generates $Q_7(x)$. Error over $[-0.8, 0.8]$: 2.44×10^{-14}.

3.4 Weber/Parabolic Cylinder Equation (Quantum Harmonic Oscillator & Plasma Stability)

The reduced equation $A_{xx} + \left(\nu + \frac{1}{2} - \frac{x^2}{4}\right) A = 0$, $(\nu = 0.3)$, models parabolic potential wells. The framework recovers $D_\nu(x)$ as A_h, and the second branch $D_\nu(-x)$ emerges from the C_6 integral. Error over $[-1,1]$: 3.63×10^{-13}.

3.5 Nonclassical Variable-Coefficient Test

To verify robustness beyond special functions, coefficients are constructed as $a_1(x) = \sin(x + 0.42)$, $a_2(x) = 2 + x^2$, $da_3(x) = 15.3e^x$. Direct numerical integration versus reduction reconstruction yields maximum errors $< 2.62 \times 10^{-7}$ for second-order, $< 7.08 \times 10^{-8}$ for third-order, and $< 2.62 \times 10^{-7}$ for fourth-order reconstructions, confirming structural stability under noncanonical coefficient profiles.

The validations are summarized in the following tables.

Table 1: The second-order benchmarks.

Model	Case	Interval	Maximum absolute error
Second order	Airy	$-2 \le x \le 2$	6.738×10^{-13}
Second order	Bessel	$0.5 \le x \le 2$	5.329×10^{-15}
Second order	Legendre	$-0.8 \le x \le 0.8$	2.442×10^{-14}
Second order	Weber	$-1 \le x \le 1$	3.634×10^{-13}

Table 2: Reconstruction errors with nonzero dependent-variable terms.

Model	Case	Interval	Maximum absolute error
Third order with nonzero dependent variable term	Airy	$-2 \le x \le 2$	1.832×10^{-15}
Third order with nonzero dependent variable term	Bessel	$0.5 \le x \le 2$	3.886×10^{-16}
Third order with nonzero dependent variable term	Legendre	$-0.8 \le x \le 0.8$	3.331×10^{-16}
Third order with nonzero dependent variable term	Weber	$-1 \le x \le 1$	3.331×10^{-15}
Fourth order with nonzero dependent variable term	Airy	$-2 \le x \le 2$	4.233×10^{-15}
Fourth order with nonzero dependent variable term	Bessel	$0.5 \le x \le 2$	2.220×10^{-16}
Fourth order with nonzero dependent variable term	Legendre	$-0.8 \le x \le 0.8$	1.110×10^{-16}
Fourth order with nonzero dependent variable term	Weber	$-1 \le x \le 1$	3.109×10^{-15}

Table 3: Non-special-function reconstruction errors.

Comparison	Maximum absolute error
Second order, variation of parameters versus direct integration	2.5544×10^{-7}
Third order original, reduction reconstruction versus direct integration	7.0761×10^{-8}
Fourth order original, reduction reconstruction versus direct integration	2.6170×10^{-7}

The proposed solution is reconstructed via reduction and then analytical solution of a second-order ODE. Reference solutions use DOP853, with numerical truncation errors small enough to lie well below the precision of the analytical solution. Initial conditions for the higher-order system are derived consistently by back-substitution through $y = e^{-\mu x}u$ and the derivative relations $g = u_x$ for third-order equations, or $g = u_{xx}$ for fourth-order equations. The results confirm that the proposed method can be used to solve compatible full higher-order variable-coefficient ODEs by reducing the problem to a second-order equation. The agreement between reconstructed analytical solutions and direct higher-order numerical integration is close to numerical precision in all tested cases. The Airy examples show that turning-point behavior is preserved by the reduction and reconstruction. The Bessel examples show that singular coefficients can be handled on intervals that do not include the singular point. The Legendre examples show that endpoint singularities can be handled on the open interval and interpreted through limiting values at the endpoints.

The framework transforms the classical problem of finding a homogeneous solution for variable-coefficient ODEs into a constructive second-order ODE. By normalizing the first-derivative term, endpoint singularities are analytically absorbed into the integrating factor. The variation of parameters step is no longer formal: the Wronskian structure emerges naturally from the C_6 integral, ensuring linear independence by construction. The method is highly amenable to symbolic algebra systems and hybrid symbolic–numeric solvers. However, the reduction applies strictly to com-

patible equations satisfying the coefficient decomposition ansatz. Not all higher-order ODEs possess this structure; irregular singular points or non-integrable coefficient couplings may violate compatibility. Nested integrals in (9c) can become computationally intensive for highly oscillatory or rapidly varying coefficients, requiring adaptive high-precision integration. Additionally, the choice of which homogeneous solution is reconstructed may admit multiple valid possibilities, necessitating consistency checks or physical boundary conditions to select the appropriate solution manifold. The formulation and validating processes are summarized in the following statement.

Theorem 1 (Compatibility–Reduction and Reconstruction)

Let $\mathscr{L}_n[y] = y^{(n)} + \sum_{k=1}^{n-1} a_k(x) y^{(n-k)} = 0$ *be a linear n-th order* ($n = 3,4$) *ODE with coefficients* $a_k \in C^\infty(I)$ *on an open interval* $I \subset \mathbb{R}$. *Suppose the coefficients satisfy the hierarchical compatibility decomposition:* $a_k(x) = b_k(x) + b_{k-1}(x)\frac{d}{dx}\ln a_k(x)$, $k = 1,\ldots,n-1$ *for smooth auxiliary functions* $a_k(x)$ *and integrating factors* $b_k(x)$. *Then:*

1. $\mathscr{L}_n[y]$ *admits an operator factorization* $\mathscr{L}_n = D^{n-2} \circ \mathscr{L}_2$, *where* $D = \frac{d}{dx}$ *and* $\mathscr{L}_2[A] = A_{xx} + f_1(x)A_x + f_2(x)A$.
2. *The homogeneous solution* A_h *of* $\mathscr{L}_2[A] = 0$ *is explicitly reconstructible via Equations (9a)–(9c) provided the compatibility condition* $Q(x) = P_x(x)$ *holds for the transformed operator.*
3. *The general solution of* $\mathscr{L}_n[y] = 0$ *follows constructively from Equation (9d), with the Wronskian determinant satisfying* $\det W[y_1,\ldots,y_n] = C\exp(-\int a_1(x)\,dx)$.

Proof The factorization follows from iterative application of the gauge transformation $u = e^{\int (a_n/b_{n-1})\,dx} y$ and the compatibility ansatz, which systematically eliminates lower-order dependent terms and exposes the derivative chain structure. The normalization $A = wB$ converts $\mathscr{L}_2$ to Liouville normal form, removing the first-derivative singularity. The substitution $B = (yZ)_x$ and integrating factor β exploit the exact derivative property of linear differential operators under compatibility, reducing the third-order Z-equation to (9a). Integration yields (9b), and inversion recovers A_h via (9c). Variation of parameters completes the basis, with Abel's identity guaranteeing linear independence and Wronskian preservation.

4 Conclusion

This paper presented a rigorous reduction and reconstruction method for compatible third- and fourth-order linear ODEs with variable coefficients. By transforming the original equation into a second-order ODE and solving it through normalization, substitution, and nested integrals (Eqs. 9a–9d), the method systematically supplies the missing homogeneous solution required for variation of parameters. Validation against Airy, Bessel, Legendre, and Weber models, including nonzero dependent-variable gauges, demonstrates agreement with classical solutions at roundoff scale. A formal compatibility–reconstruction theorem establishes the analytical foundation, while a critical evaluation highlights singularity regularization, computational structure, and domain applicability.

The results confirm that resolving the second-order analytical problem is the key step in making Wronskian higher-order reduction constructive and exact. The third- and fourth-order reductions suggest a promising and natural extension to higher-order systems. We formalize this extension through the following conjecture and proposition.

Conjecture 1 (Iterative Compatibility Reduction for n-th Order Systems)

Any linear n-th order ODE with variable coefficients ($n \geq 5$) that satisfies a hierarchical compatibility decomposition of the form $a_k(x) = b_k(x) + b_{k-1}(x)\frac{d}{dx}\ln a_k(x)$, $k = 1,\ldots,n-1$, can be reduced to a second-order equation through successive operator factorizations $\mathscr{L}_n = D^{n-2} \circ \mathscr{L}_2$, where each reduction step eliminates one derivative order via an exponential transformation and coefficient matching. The homogeneous solution of $\mathscr{L}_2$ reconstructs the full solution space of $\mathscr{L}_n$ via $n-2$ successive integrations, preserving linear independence and Wronskian structure.

Proposition 1 (n-th Order Reconstruction)

If the reduced second-order ODE admits a homogeneous solution g_h *via Equations (9a)–(9c), then the original n-th order solution* $y(x)$ *is given by* $y(x) = e^{-S_{n-2}(x)} \underbrace{\int \cdots \int}_{n-2 \text{ times}} g(x)\,dx^{n-2}$, *where* $S_{n-2}(x) = \sum_{i=1}^{n-2} \int s_i(x)\,dx$ *accumulates the integrating functions from each reduction step, and* $g(x)$ *is the general solution of the second-order equation. The reconstruction preserves the Abel–Liouville Wronskian identity:* $\det W[y_1,\ldots,y_n] = C\exp(-\int a_1(x)\,dx)$.

References

1. E. A. Coddington and N. Levinson, *Theory of Ordinary Differential Equations*, McGraw–Hill, New York, 1955.
2. E. L. Ince, *Ordinary Differential Equations*, Dover Publications, New York, 1956.
3. NIST Digital Library of Mathematical Functions, "Airy, Bessel, Legendre, and Parabolic-Cylinder Functions," National Institute of Standards and Technology, available at https://dlmf.nist.gov.

4. M. Abramowitz and I. A. Stegun, *Handbook of Mathematical Functions with Formulas, Graphs, and Mathematical Tables*, National Bureau of Standards, 1964.
5. M. J. Fogaça and E. L. Cardoso, "A Systematic Approach to Obtain the Analytical Solution for Linear Second Order Ordinary Differential Equations: Part I," *Journal of the Brazilian Society of Mechanical Sciences and Engineering*, 2024, DOI: 10.1007/s40430-024-04755-8.
6. P. Zheng, J. Luo, S. Li and X. Dong, "Elastic Transformation Method for Solving Ordinary Differential Equations with Variable Coefficients," *AIMS Mathematics* **7**(1) (2022), 1307–1320, DOI: 10.3934/math.2022077.
7. M. A. Jama, K. Giterere and D. G. Kioi, "A Novel Analytic Method with Integral Transform for Solving Classes of Second and Third Order Ordinary Linear Differential Equations with Variable Coefficients," *Applied and Computational Mathematics* **14**(2) (2025), 78–89, DOI: 10.11648/j.acm.20251402.11.
8. M. Gadella and L. P. Lara, "A Note on Linear Differential Equations with Variable Coefficients," *arXiv preprint*, arXiv:2410.08630 (2024), DOI: 10.48550/arXiv.2410.08630.
9. E. Capelas de Oliveira and J. E. Maiorino, "Ordinary Differential Equations," in *Analytical Methods in Applied Mathematics*, Springer Nature, 2025.
10. J. Lebl, "Higher Order Linear ODEs," *Mathematics LibreTexts*, updated 2025, https://math.libretexts.org.
11. SciPy Developers, "`scipy.integrate.solve_ivp` Documentation," SciPy API Reference, https://docs.scipy.org, accessed 2026.
12. E. Hairer, S. P. Nørsett and G. Wanner, *Solving Ordinary Differential Equations I: Nonstiff Problems*, 2nd ed., Springer, 1993.